Aeroacoustics Conferences
20-23 May 2019, Delft, The Netherlands
25th AIAA/CEAS Aeroacoustics Conference

10.2514/6.2019-2403

Fundamental Studies of the Mechanisms of Pressure Shielding

Alexander J. Gonzalez,[1] and Stewart Glegg [2]
Department of Ocean and Mechanical Engineering, Florida Atlantic University, Boca Raton, FL 33431, USA

Nandita N. Hari[3], Marika Ottman[4] and William J. Devenport[5]
Center for Research in Experimental Aero/hydrodynamic Technology (CREATe), Department of Aerospace and Ocean Engineering, Virginia Tech, Blacksburg, VA 24061, USA

Previous studies have demonstrated that structures such as a canopy or finlets placed within a boundary layer over an aerodynamic surface can attenuate pressure fluctuations on the surface without compromising aerodynamic performance. This paper describes research into the fundamental mechanisms of this pressure shielding. Experiments and analysis are performed on elemental canopy configurations (parallel arrays of streamwise rods) that eliminate the confounding effects of a leading-edge support structure. Experiments show that such a canopy produces attenuation in two distinct frequency ranges. At low frequencies (convective scales much greater than the canopy height) attenuation spectra scale on the canopy height Strouhal number, but at high frequencies (canopy scales of the order of the height) a dissipation type frequency scaling appears more appropriate. RANS calculations are performed simulating the canopy geometry directly and as a porous layer. Pressure fluctuation spectra predicted from the RANS results by separately accounting for inner and outer layer contributions are able to accurately recreate the wall pressure spectra both with and without the canopy and thus the major features of the attenuation spectra.

I Introduction

This paper is concerned with understanding the fundamental physical and mathematical basis for treatments that shield aerodynamic surfaces from turbulent pressure fluctuations, while maintaining the wall-normal transport of momentum and low drag that are required in most fluid dynamic applications.

Reducing surface pressure fluctuations produced by turbulent flows is highly desirable. Surface pressure fluctuations serve as the excitation for major sources of flow noise such as the trailing edge noise that dominates the sound from wind turbines and the leading-edge noise of helicopter rotors. Surface pressure fluctuations contaminate sound measurements made with surface-mounted instrumentation limiting usefulness of acoustic sensors in active flow control, environmental monitoring and surveillance applications. Surface pressure fluctuations are the driver behind fluid structure interaction and serve as the source term for panel vibrations, which are an important component of cabin noise in passenger aircraft or the interior wind noise in cars. On an atmospheric scale, surface pressure fluctuations are directly related to wind gust magnitude that can cause damage to structures.

Recent studies, reviewed below, have definitively demonstrated that pressure shielding is possible, and can be effective not only in controlling surface pressure fluctuations but in attenuating some of their undesirable effects. These studies have drawn on a combination of biological inspiration and heuristic methods to design effective treatments. They have provided a first indication of some of the physics behind how pressure shielding may work. None of these prior efforts, however, have provided quantitatively usable fundamental understanding of the mechanisms, nor the mathematical methods needed for their prediction.

The overarching objectives of this research effort are:

1) To reveal through combined experimental, theoretical and computational work the fundamental mechanisms of pressure shielding
2) To develop flow models that can be used for the quantitative prediction of pressure shielding effects on both the spatial correlations and spectral characteristics of wall pressure fluctuations

[1] Graduate Research Assistant.
[2] Professor, Associate Fellow AIAA.
[3] Graduate Research Assistant.
[4] Undergraduate Researcher
[5] Professor, Associate Fellow AIAA.

In this paper, we present experimental and computational results that represent the first stage of this work. These studies have been focused on the fundamental configuration of the unidirectional rod-canopy and have investigated its pressure-shielding properties when immersed in a wall jet boundary layer.

II Background

Recent research, beginning with Clark *et al* . (2016), has shown that pressure shielding is a practical possibility. They considered the use of fabric canopies as a means to shield surface roughness from an over-riding turbulent flow with the goal of reducing surface pressure fluctuations on the roughness and therefore roughness noise. They found that canopies made from a parallel array of streamwise oriented fibers (Figure 1), with an open area ratio of 70% to be most effective. Their experiments were conducted in a wall jet and the fibers were placed about 40% of the boundary layer thickness from the wall. They found that the fibers attenuated surface pressure fluctuations by over 20dB at higher frequencies. Attenuation increased with frequency approximately exponentially at higher frequencies. In their analysis they were able to model some aspects of the pressure attenuation, its frequency and flow speed dependence, based on the hypothesis that the canopy introduces a new shear layer that displaced the generation of pressure-producing instabilities away from the wall.

Shear sheltering was first articulated by Jacobs and Durbin (1998) in the context of laminar boundary layer susceptibility. They found that free stream disturbances failed to significantly penetrate the boundary-layer shear, despite their associated pressure perturbations. Hunt and Durbin (1999) then expanded this idea to include a variety of different types of shear layers. Shear sheltering has since been invoked in many applications, from the control of ionized plasma flows (Kwak et al. 2017), to the understanding of interactions between forest canopies and the atmosphere (Prabha et al. 2007), the fluid dynamics of wind flow over crops (Raupach et al. 1996, Finnigan 2000, Belcher et al. 2012), and rough-wall boundary layers (Belcher et al. 2003) but none of these have been concerned with wall pressure fluctuations.

A second possible mechanism is the spectral shortcut. This is the enhancement of dissipation, and thus the transfer of energy from large to small scales by the presence of a solid structure that generates intense turbulence on a small scale. Examples here include the screens of wind tunnel, the flow through dense vegetation (Finnigan 2000) and, perhaps, the fine hairs on the wings of silent flying owls (Lilley 1998). In the context of Clark *et al.*'s experiment, the breakup of large-scale eddies at the fiber canopy could have generated small scale turbulence with pressure fluctuations that would have been rapidly attenuated before reaching the wall.

To be useful in most fluid dynamic applications, the reduction of wall pressure fluctuations must be accomplished without increasing the susceptibility of a boundary layer to separation, or incurring too great a drag penalty. In a follow up study, Clark *et al.* (2016, 2017) established this by adapting their fiber canopy configuration for use as a surface treatment at the trailing edges of airfoils. Their goal was the reduction of trailing edge noise by suppressing pressure fluctuations at the trailing edge. Some 20 different treatment configurations were attempted based on two designs. Both designs were surprisingly successful both in reducing trailing edge noise at higher frequencies, in many cases by as much as 10dB. Direct measurements made in selected cases showed these reductions were directly tied to reductions in the intensity of pressure fluctuations at the trailing edge, as intended. Airfoil lift was not significantly impacted, even approaching stall, and the treatments only produced a small increase in drag, approximately equivalent to the increase in wetted area. The pressure shielding was therefore achieved without sacrificing the aerodynamic robustness of the boundary layer.

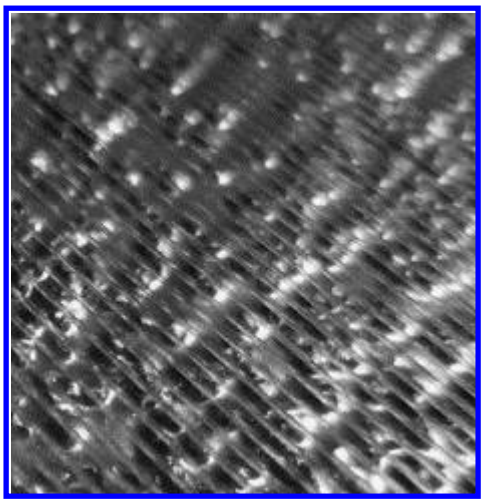

Figure 1. Streamwise oriented fibers used to provide pressure shielding of a rough surface immersed in a turbulent boundary layer. Clark et al. (2016)

Subsequent studies of the finlet configuration conducted by Ashfari *et al.*(2016, 2017), Bodling *et al.*(2017, 2017, 2018), and Millican *et al.* (2017, 2017), have provided further insight into the mechanisms involved. Ashfari *et al.*(2016, 2017) studied the flow of a turbulent boundary layer on a flat plate with a series of different finlet configurations up to about $1/6^{th}$ of the boundary layer thickness in height. They varied spacing, height and pattern. Measurements made downstream of the finlets showed that they decreased pressure fluctuation intensities on the plate at high frequencies and reduced pressure correlation scales and near wall velocity fluctuations. The finlets slowed down the near wall flow, reducing convection velocities here, while increasing velocity gradients and turbulence levels around the top of the finlets. Millican *et al.* (2017) and Millican (2017) made velocity and turbulence measurements at the immediate exit of rows of finlets and rails placed in a wall jet boundary layer. They showed the formation both

of a shear layer at the finlet/rail height as well as enhanced turbulence levels as might be expected from shear layer turbulence production, or a spectral shortcut mechanism mediated by the no-slip condition imposed by the treatment. Bodling *et al.*(2017, 2017, 2018) used large eddy simulation to model the flow over a NACA 0012 airfoil both with and without finlets installed at the trailing edge. Their calculations confirmed that the finlets have no significant impact on the aerodynamic performance of the airfoil, but at the same time reduce pressure fluctuations at high frequencies. Gonzalez (2019) used RANS calculations to model homogenous porous canopies and rod canopies in a wall jet boundary layer. Analysis of the surface pressure fluctuations showed that increased acoustic performance was dependent upon reducing the velocity shear and turbulence near the wall.

Overall, these studies of pressure shielding show a consistent but not entirely clear picture. In all cases the pressure shielding is accompanied by enhanced turbulent activity at the height of the effective canopy as well as the formation of a shear layer there, and some reduction velocities beneath the canopy level. These are features consistent both with the shear sheltering mechanism and with the spectral short cut mechanism. Furthermore, all the above studies have examined configurations that produce an effective canopy at some distance from a wall, but in the presence of some leading-edge structure through which the flow beneath the canopy must first pass. Thus it is not clear in these studies the extent to which these two components are separately responsible for the observed pressure shielding. In the present study we have attempted to separate the canopy effect.

In the remainder of this paper we investigate the pressure shielding phenomenon first through dimensional analysis (section III), then experimental pressure fluctuation measurements (section IV) and the computational and analytical studies (section V). Our conclusions (section VI) include the observations that pressure shielding scales in ways that are consistent both with shear sheltering and the spectral shortcut and that the pressure attenuation can be successfully modelled using RANS calculations and a two-scale wall pressure spectrum model.

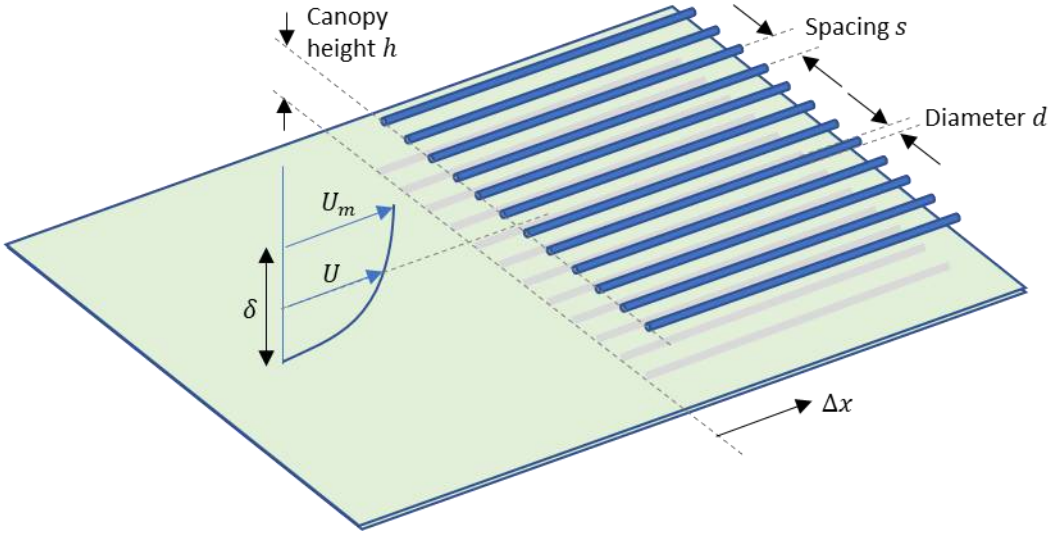

Figure 2 Schematic of a rod-canopy placed at a height over a wall in a boundary layer

III Observations Concerning Scaling

Consider a canopy without a leading-edge structure idealized as a set of evenly spaced streamwise oriented rods with diameter, d and spacing s, measured between the centers of the rod cross-sections. Let h be the height of the canopy from the wall and Δx the distance of the measurement point from the canopy leading edge. Assuming the canopy is placed in a boundary layer, the flow can be characterized by the mean velocity at the canopy leading edge U_h and the edge velocity of the boundary layer U_m and its thickness δ. The pressure attenuation at the wall can be defined as a function of the flow and geometric variables. Overall, we expect the pressure fluctuation in the presence of the canopy p' to have the functional form:

$$\boldsymbol{p' = f(p'_{nc}, U_h, U_m, \delta, \nu, d, s, h, \Delta x, \omega)} \tag{1}$$

where ω and ν are frequency and kinematic viscosity and p'_{nc} is the wall pressure fluctuation that would be experienced in the absence of the canopy. This, of course, is not an exhaustive variable list but includes the parameters we expect to be most important. Using Buckingham Pi theorem, the above equation can be expressed in terms of the non-dimensional parameters seen in equation 2.

$$\frac{p'}{p_{nc'}} = F\left(\frac{\Delta x}{h}, \frac{s}{d}, \frac{\omega h}{U_m}, \frac{\omega \nu}{U_h^2}, \frac{U_h d}{\nu}, \frac{\delta}{h}, \frac{U_h}{U_m}\right) \tag{2}$$

Of course, this is only one set of possible parameters, though we have selected those we expect to be most meaningful. Included in this list are s/d, representing the open area ratio $(1 - d/s)$ and the normalized distance from the canopy leading edge $\Delta x/d$ that we would expect to control initial behavior associated with the canopy leading edge. Implicit in equation 2 are the Reynolds numbers based on rod spacing, height from wall, and streamwise distance from the canopy leading edge. A key part of our study is to find the impact of these parameters individually or in combinations and develop a relation for the purpose of understanding the physics behind the pressure shielding mechanism.

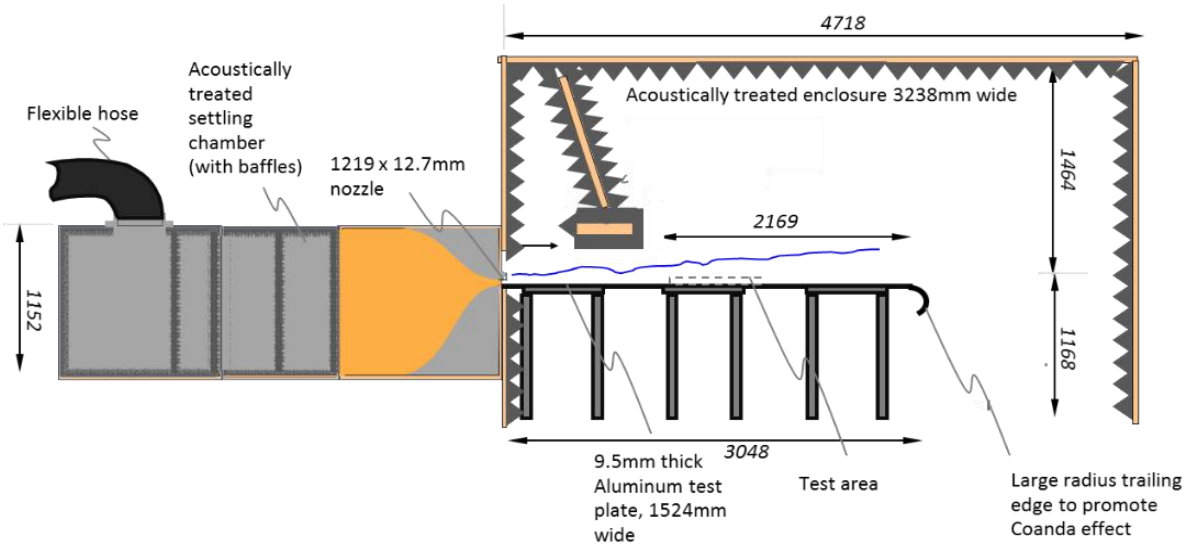

Figure 3 Schematic of the Wall Jet Wind Tunnel. All measurements are shown in mm.

IV Experimental Studies

Experimental studies were performed using canopies closely approximating the configuration of Figure 2. The effect of these canopies on surface pressure fluctuations at different configurations and flow speeds were investigated. Flow measurements were performed in the Virginia Tech Anechoic Wall-Jet facility with the help of surface microphones mounted on the wall plate.

IV.A Apparatus and Instrumentation

Anechoic Wall-Jet Wind Tunnel Facility

The low-speed Anechoic Wall Jet facility at Virginia Tech, re-built recently (Kleinfelter *et al.* 2019), produces a quiet environment for studying fully turbulent boundary layer flows using various flow measurement techniques and devices. The wall jet is composed of a boundary layer near the wall and a mixing layer beyond, which allows for both surface and far-field measurements over a range of controlled aerodynamic conditions. A schematic of the Anechoic Wall-Jet Wind Tunnel is shown in Figure 3. The flow generated by a centrifugal fan passes through a discharge silencer and flexible rubber hose to an acoustically treated settling chamber. The flow then gets accelerated through a contraction section and exhausted from 12.7 mm high and 1219 mm wide nozzle onto a 3.05-m long wall plate placed in an anechoic chamber as shown in figure. The facility is capable of producing jet exit velocities, U_j, typically ranging from 20 m/s to 70 m/s within ± 0.1 m/s.

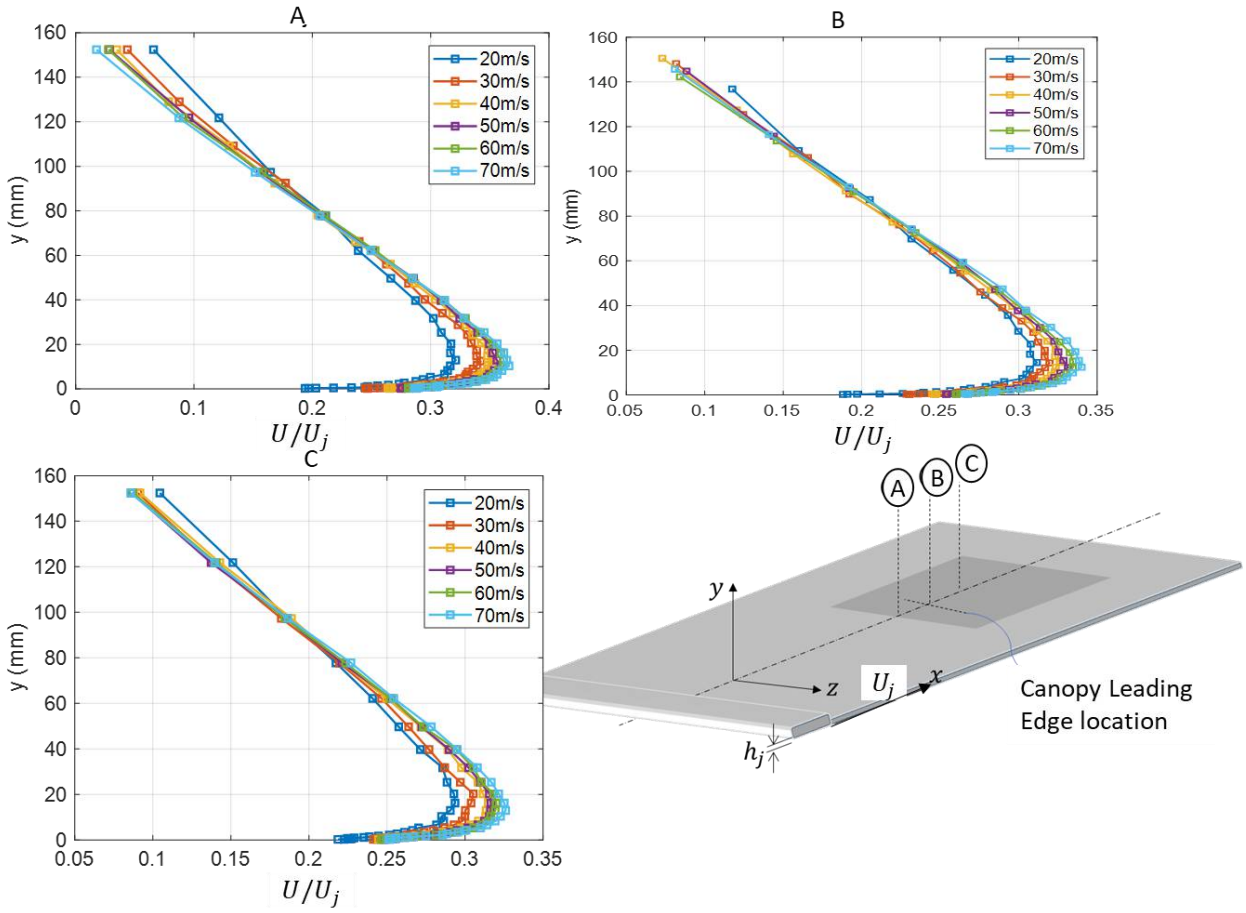

Figure 4 Mean velocity profiles measured on the wall jet centerline as a function of jet exit velocity $\mathbf{U_j}$

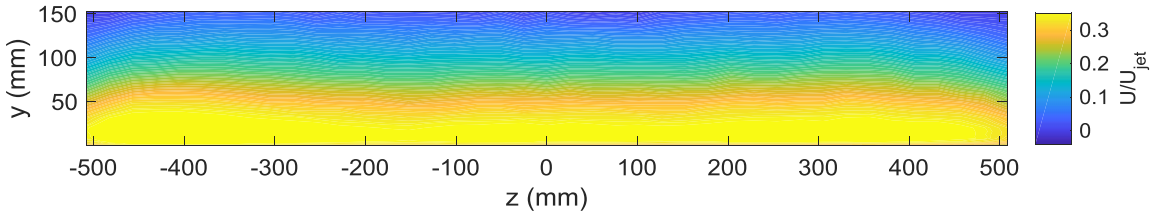

Figure 5 Cross-Sectional mean velocity contour measured 0.15m upstream of Canopy leading edge at x=1.13m at jet velocity of 70 m/s (Kleinfelter et al. 2019)

Figure 4 shows the centerline evolution of the wall-jet mean velocity profile at three downstream locations $x = 1.13, 1.28$ and 1.43 m respectively, where x is the streamwise distance measured from the origin. The origin of the coordinate system is the nozzle exit plane, with the positive x-axis facing downstream, positive y-axis as wall upward normal and the z-axis centered spanwise, following the right-hand coordinate system. The flow attains a fully developed state before it reaches the test area, starting at $x = 1.13m$ marked by the shaded region. The canopy is placed on the wall such that its leading edge is at $x = 1.28$ m which corresponds to location B in the same figure. Boundary layer profiles at the corresponding three downstream locations are shown by plotting distribution of mean velocity along the y-direction. Figure 5 shows the cross-sectional velocity distribution at $x = 1.13\ m$ which is 0.15m upstream of the canopy leading edge location. We observe the mean velocity to be relatively uniform and two-dimensional across 800mm in the spanwise direction. When placed into the flow, the mid-span of the canopy was aligned with z=0, so that the entire 0.3-m width of the canopy would lie well within the spanwise-uniform region. The self-similar form of the undisturbed wall jet mean-velocity profile is well defined by the scaling formulation proposed by Wygnanski *et al.* (1992) for a fully developed wall-jet flow as:

$$\frac{U_m}{U_j} = A_U Re_j^{n+1} Re_x^n \tag{3}$$

$$\frac{\delta^*}{h_j} = A_D Re_j^{p-2} Re_x^p \tag{4}$$

$$\theta = B\delta^* \tag{5}$$

$$\delta = A\delta^* \tag{6}$$

Where; U_j is the jet velocity, δ^* is the displacement thickness, θ is the momentum thickness, δ is the boundary layer thickness and U_m is the maximum velocity in the boundary layer, also referred as wall jet boundary layer edge velocity. Re_j and Re_x are Reynolds numbers based on nozzle height and streamwise distance respectively. Constants A_U,A_D, $A, B, n,$ and p were determined from wall jet mean velocity measurements and are shown below in Table 1. Given these constants, the boundary layer parameters U_m, δ^* *and* δ can be calculated at any downstream location. Boundary layer parameters for canopy leading edge position ($x = 1.28m$) are given in *Table* 2.

Table 1: Wall jet constants (Kleinfelter et al. 2019)

$\boldsymbol{A_U}$	1.497
$\boldsymbol{A_D}$	0.0049
$\boldsymbol{A}$	16.012
$\boldsymbol{B}$	0.8387
$\boldsymbol{n}$	-0.4684
$\boldsymbol{p}$	0.9232

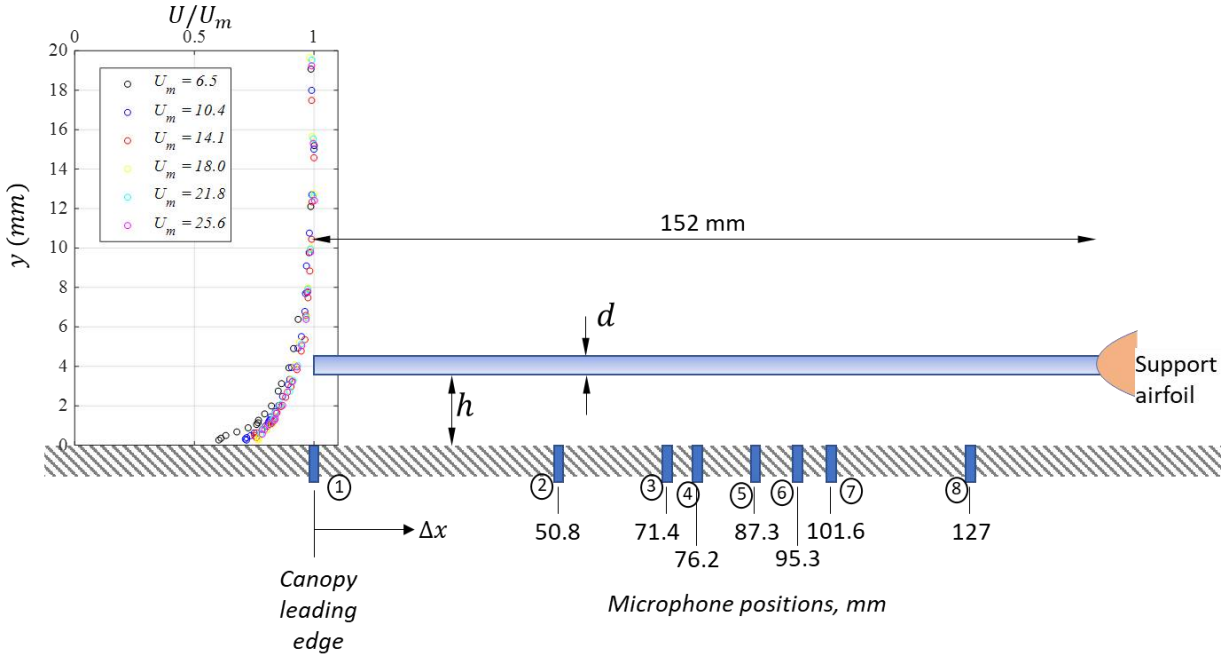

Figure 6 Canopy arrangement and microphone positions for the horizontal canopy measurements. Mean velocity profiles show undisturbed flow at the canopy leading edge inferred from profiles measured at x=1.13 m using the wall-jet similarity scaling

Table 2: Flow properties computed at streamwise distance at canopy leading edge

$U_j(m/s)$	$U_m(m/s)$	$\delta(mm)$	$\delta^*(mm)$
20	6.34	16.0	1.00
30	9.75	15.1	0.94
40	13.24	14.4	0.90
50	16.8	13.9	0.87
60	20.4	13.6	0.85
70	24.01	13.2	0.82

Mean-velocity profiles showing the undisturbed flow at the canopy leading edge location are shown in Figure 6. These are inferred from profiles measured at x=1.13 m scaled using the wall-jet similarity relations above. Turbulence intensity profiles measured in the near-identical flow of the predecessor wall jet tunnel (Devenport et al. 2011) show streamwise turbulence intensity almost constant across the boundary layer portion of the wall jet with a level or around 14% of U_m.

Instrumentation

Reference conditions

The jet exit velocity was measured at the nozzle exit by measuring dynamic pressure based on total pressure in the settling chamber and ambient pressure inside the test chamber. Tygon tubes from both locations are connected to $\pm$ 3.75 kPa-range Setra 239 pressure transducer that reads a differential pressure with an uncertainty of $\pm$ 2.7 Pa. This transducer was connected to an NI-DAQ which fed data to an in-house MATLAB program. Atmospheric pressure was provided from local meteorological conditions, corrected for the appropriate elevation. Flow temperature was measured with a thermocouple connected to Omega DP86T analog output with an uncertainty estimated to be 0.1^oCelcius. The thermocouple is placed at the edge of the nozzle such that its tip is in the flow without causing any disturbance.

Surface pressure measurements

Measurement of the surface pressure spectra was done with a series of eight Knowles electret microphones (FG-23329-P07) mounted flush to the wall. These microphones have a circular sensing area of 0.76 mm, with a flat frequency response between 100 Hz-10 kHz. Surface pressure fluctuations were measured at eight downstream locations at $z = 0$ under the canopy mid-span to understand downstream evolution of the canopy effect. Figure 6 shows the experimental setup consisting of a horizontal canopy placed at height $h = 4mm$, with incoming undisturbed flow profile as seen by the canopy leading edge. Distance of each microphone measured from the canopy leading edge is shown. The canopy was placed such that microphones were centered spanwise in the gap between adjacent rods of the canopy. The microphone x spacing was chosen to obtain multiple relative distances for correlation analysis.

Since the Knowles microphones have a pinhole cap, we calibrated them using B&K $1/8''$ microphone with standard salt and pepper cap to identify their frequency response. An Agilent E1432 digitizer and an ID60C8 speaker were used to emit white noise 1.7 m away from the microphone location, and the entire setup was placed in the anechoic chamber of the wall jet. Sensitivity of the reference B&K microphone was determined by pistonphone calibration at 251.2 Hz.

Microphone data was acquired using six-channel Bruel and Kjaer Type 3050 24-bit LAN-XI module sampled at 65536 Hz. To process the time series data, Fast Fourier Transform of the data was performed for sections of records of length 8192 multiplied by a Hanning Window with 50% overlap. Absolute pressure fluctuation levels are presented in terms of Sound Pressure Level (SPL) in units dB/Hz defined by:

$$SPL = 10\log_{10}\left(\frac{G_{pp}}{p_{ref}^2}\right) \tag{7}$$

Where G_{pp} is the one-sided spectral density (Pa^2/Hz), and p_{ref} is $20\mu Pa/\sqrt{Hz}$. The attenuation in surface pressure fluctuations is calculated as ΔSPL which gives the effectiveness of a canopy, obtained by subtracting pressure fluctuation SPL levels measured on the smooth wall without the canopy present, from those measured in the presence of canopy, i.e.

$$\Delta SPL = 10\log_{10}\left(\frac{G_{ppnocanopy}}{G_{pp_{canopy}}}\right) \tag{8}$$

Uncertainty in the measured pressure spectral density was 2.2dB at a jet exit velocity of 20 m/s and 1.4 dB at 70 m/s accounting for 0.5dB, due to placement of microphone, 1dB (20 m/s) to 0.2 dB (70 m/s), due to the flow conditions, 0.25 dB due to uncertainty of the measurement system and 0.5 dB due to calibration uncertainty.

Uncertainty induced due to flow conditions were obtained by observing repeated runs and was found to be associated with flow speed. Calibration uncertainty was obtained by looking at repeated calibrations of microphone measurements. We observed a reduction in the uncertainty with increasing jet speed.

Canopy Design

An evenly spaced array of rods was placed streamwise to recreate the essential features of unidirectional fiber canopies of Clark *et al* (2016). Stiff rods were chosen over previously used fibers because they can be supported from downstream and therefore eliminate the influence of any leading-edge structure. Another advantage of the design was the ability to tilt the canopy to any required angle in order to simulate leading edge structure effects. The baseline configuration was designed to most closely mimic the fibers of the unidirectional Canopy 3 of Clark *et al.*

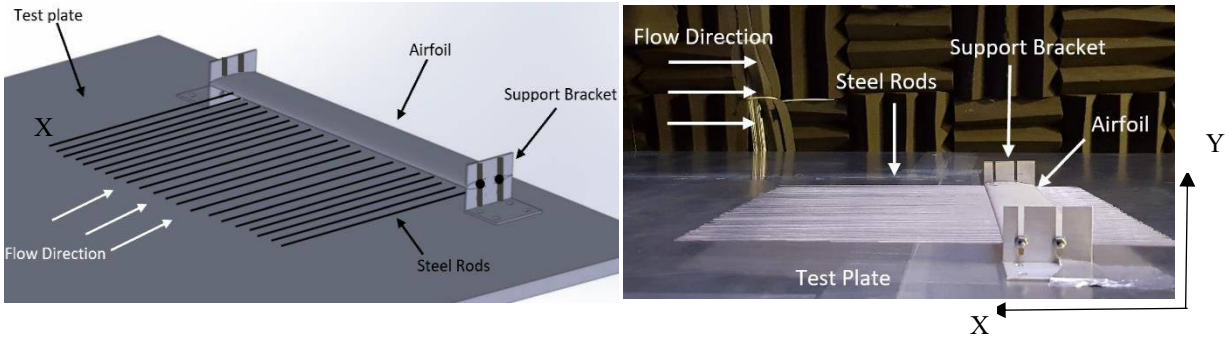

Figure 7 (a) Schematic of canopy with the support structure placed on the wall (b) Image of canopy placed at parallel to the wall in the wall jet

Each canopy is composed of uniformly spaced stainless-steel rods which are cantilevered to an airfoil shaped mounting strut as shown in Figure 7. The airfoil acts as a support and is held in place by 50mm x 50mm L-brackets on either side. This design allows us to alter the geometric parameters of diameter, spacing and the canopy height individually therefore, making it possible to analyze the effect of several non-dimensional parameters independently. Spacing is defined as the distance from the mid-point of one rod to the mid-point of the adjacent rod. The height for the experimental studies has been calculated as the distance from the wall to the bottom of the rod. Another important parameter used to characterize a canopy is the open-area ratio, given as $(s-d)/s$. The density of the canopy can be altered by changing the spacing or diameter of the rod and correspondingly altering the airfoil support. This design also allows the airfoil to pitch about the z-direction where the canopy is tilted thus making it possible to separate canopy effects from entrance condition effects. Three configurations of canopies were fabricated as shown in Table 3.

Table 3 Geometric parameters of the three canopies

Canopy Configuration	Rod Length $(\mathbf{mm})$	Rod Diameter $\boldsymbol{d}$ $(\mathbf{mm})$	Spacing $\boldsymbol{s}$ $(\mathbf{mm})$	Open-Area Ratio, $(\boldsymbol{s-d})/\boldsymbol{s}$
1	152.4	1.00	3.00	0.66
2	152.4	1.58	4.76	0.66
3	152.4	1.00	4.00	0.75

The airfoil and brackets were designed to be aerodynamic to minimize the disturbance caused to the flow. A Selig S12012 HPV airfoil, symmetrical with relatively flat upper and lower surfaces was chosen. The airfoil strut had a chord length of 50.8 mm, thickness of 6.1 mm and 304.8 mm span. Rods were smoothed at the ends and push-fit into streamwise holes in the strut with centers at an offset of 2.54 mm below the airfoil center-line. The length of the rods was limited by the need to avoid significant deflection and vibration effects at the highest flow speed at 70 m/s. The set-up also allows for the rod lengths to be adjusted relative to the airfoil.

Test Cases

The three canopies of Table 3 were each tested in the wall-jet boundary layer flow surface at heights h of 2mm, 4mm, 6mm, 8mm, 12mm and 15mm. For each height, measurements were made for jet exit velocities ranging from 20 m/s to 70 m/s, in increments of 10 m/s, corresponding to boundary layer edge velocities at the canopy leading edge of 6.3 to 24 m/s given in Table 2. For each height and velocity, surface pressure fluctuation measurements were made at each of the 8 microphone locations depicted in Figure 6. The resulting set of geometric parameters studied is shown in Table 4. Each row in the table corresponds to the particular height, h tested, and each case within the row corresponds to a streamwise measurement location below the canopy. Corresponding measurements in all cases were

made of the unmodified wall-jet with the canopy assembly removed. Measurements were also made with the canopy removed but with its support structure (airfoil strut and L brackets) in place.

Table 4: Test cases for three canopy configurations and the associated non-dimensional geometric parameter, in all cases measurements were made at speeds of U_j =20 to 70 m/s, corresponding to boundary layer edge velocities of 6.3 to 24 m/s

				Configuration 1 $\frac{s-d}{d}=0.66$		**Configuration 2** $\frac{s-d}{d}=0.66$		**Configuration 3** $\frac{s-d}{d}=0.75$	
CASES	h (mm)	Mic position measured from canopy LE, Δx (mm)	$\Delta x/h$	s/h	d/h	s/h	d/h	s/h	d/h
1-8	2	0, 50.8, 71.4, 76.2, 87.3, 95.3, 101.6, 127	0, 25.5, 35.8, 38.2, 43.8, 47.8, 50.9, 63.7	1.5	0.50	2.34	0.78	2.00	0.50
9-16	4	0, 50.8, 71.4, 76.2, 87.3, 95.3, 101.6, 127	0, 12.7, 17.9, 19.1, 21.9, 23.9, 25.5, 31.8	0.75	0.25	1.17	0.39	1.00	0.25
17-24	6	0, 50.8, 71.4, 76.2, 87.3, 95.3, 101.6, 127	0, 8.5, 11.9, 12.7, 14.6, 15.9, 16.9, 21.2	0.5	0.17	0.78	0.26	0.67	0.17
25-32	8	0, 50.8, 71.4, 76.2, 87.3, 95.3, 101.6, 127	0, 6.4, 9.0, 9.6, 10.9, 11.9, 12.7, 15.9	0.375	0.125	0.585	0.195	0.50	0.125
33-40	12	0, 50.8, 71.4, 76.2, 87.3, 95.3, 101.6, 127	0, 4.2, 6.0, 6.4, 7.3, 8.0, 8.5, 10.6	0.25	0.08	0.39	0.13	0.33	0.08
41-48	15	0, 50.8, 71.4, 76.2, 87.3, 95.3, 101.6, 127	0, 3.4, 4.8, 5.1, 5.8, 6.4, 6.8, 8.5	0.2	0.07	0.312	0.104	0.27	0.07

IV.B Results and Discussion

Pressure spectra of the undisturbed wall jet

Surface pressure spectra were measured for six different wall jet velocities corresponding to wall-jet boundary layer edge velocities of 6.3 to 24 m/s, calculated at canopy leading edge. Figure 8 compares the autospectra measured at $x = 1.28m$, which is the canopy leading edge position, for all tested velocities. Sound Pressure Level, in dB is plotted on the vertical axis against frequency (Hz) on the horizontal axis. We observe the spectral data is described by three distinct frequency ranges. First, low-frequency region, below about 1 kHz at 24 m/s, the spectra shows high amplitude fluctuations indicative of the large scale and high energy structures present in the outer mixing layer. Mid-frequencies, from 1 kHz to about 3-6 kHz (depending on the velocity), show a slope of approximately -0.8, for all tested flow speeds. The high-frequency region ranging from 3 to 6 kHz, shows a rapid reduction in the spectral amplitude with frequency, indicative of a typical energy cascade mechanism in a turbulent boundary layer and the viscous dissipation of the smallest turbulent scales.

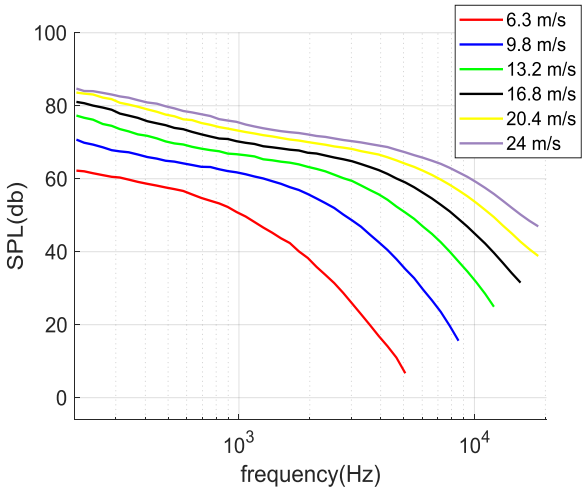

Figure 8 Surface pressure spectra measured at $\boldsymbol{x}$ =1.28 m as a function of boundary layer edge velocity $\boldsymbol{U_m}$

Surface pressure spectra scaled on inner and outer variables respectively as shown in Figure 9. The inner variables chosen were ν/u^*, u^* and τ_w which approximately scale the high frequency region from non-dimensional frequency of $\omega\nu/u^{*2} = 10^{-2}$ and beyond. Here u^* and τ_w are respectively the friction velocity and wall shear stress obtained from the Bradshaw and Gee (1962) correlation. Outer scaling variables, δ, U_m and τ_w should scale the spectra at non-dimensional low frequencies up to $\omega\delta/U_m$=10 (Smith (2008)). However, at low non-dimensional frequencies $\omega\delta/U_m$< 2, spectra for the U_m = 20.4 and 24 m/s cases fall

below those at other speeds for reasons that are not yet understood. Both scalings show a collapse to within 5dB and also seem to scale the mid-frequency overlap region. Increasing the flow speed and Reynolds number results in higher energy content in the flow which in turn causes high pressure fluctuation levels. Also, increasing speed results in higher convective speed over the microphone and decreasing scale at which viscous dissipation occurs, and therefore a shift in the frequency can be observed in the dimensional spectra.

Effects of the Canopy Supports

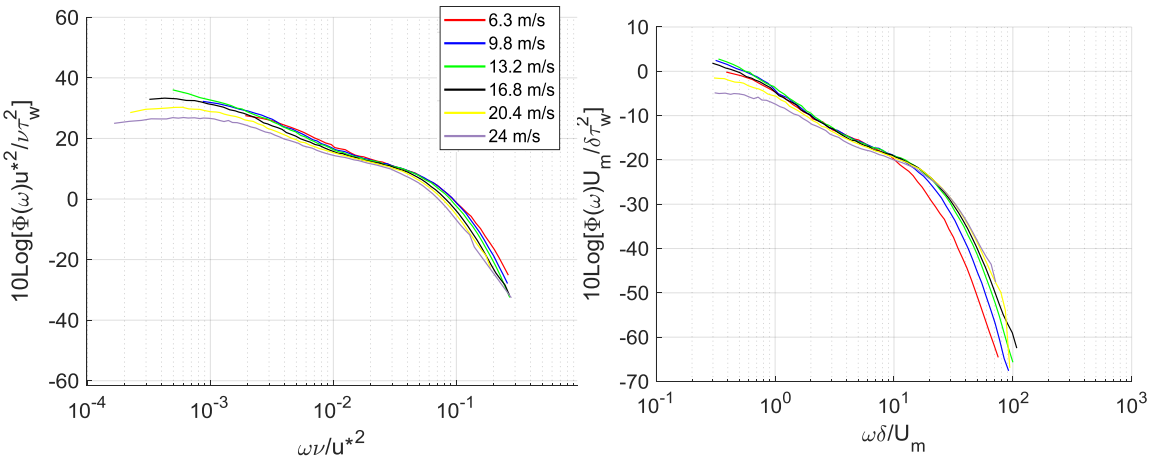

Figure 9. Smooth wall pressure spectra scaled using inner (ν, u^* and τ_w) and outer variables (δ, U_m and τ_w) respectively

In order to study the upstream influence of the support structure on surface pressure measurements, comparison studies were performed. Clean wall measurements were compared with measurements made with the canopy support structure (but no canopy) placed on the wall. Experiments were performed at jet velocities corresponding to wall jet boundary layer edge velocity ranging 6.3 to 24 m/s and support structure positions corresponding to all the canopy heights mentioned in Table 4. Effects of the canopy support structure on the wall pressure spectrum were only observed at the most downstream microphone location Δx =127 mm (25 mm upstream of the airfoil strut leading edge), and these effects were slight. Figure 10 shows these effects for supports at varying heights. At high frequencies support structure effects are seen in the roll off of the spectrum and reduce with increasing speed and height. The maximum effect of the airfoil is therefore felt at 2mm height and 6.3 m/s. Effects are visible at low frequencies at 20.4 m/s. Effects at all other microphone locations were within the measurement uncertainty. In all cases, attenuation effects were determined by taking the ratio of measured wall pressure spectra without the supports present.

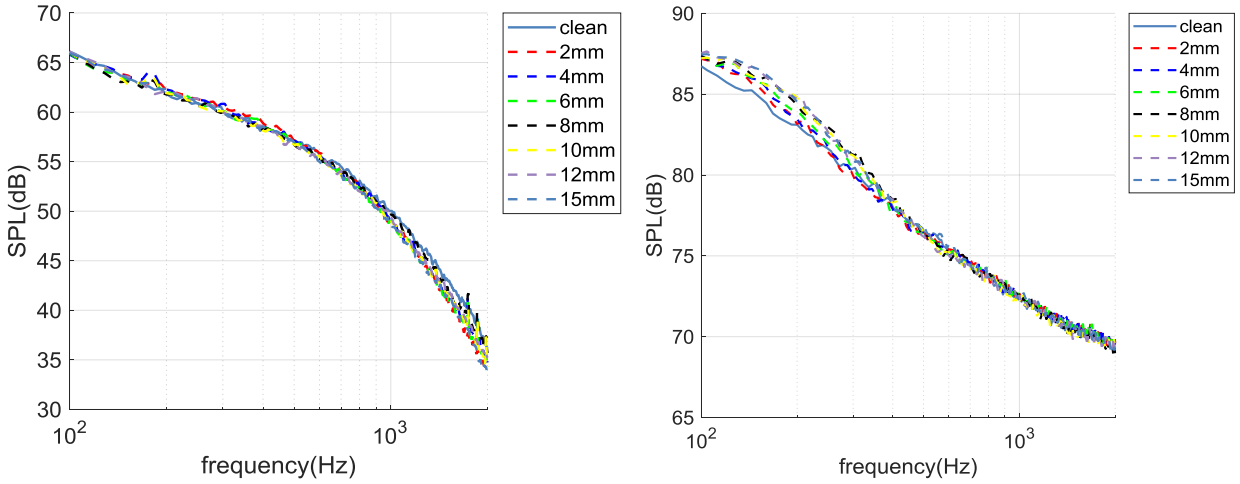

Figure 10 Effect of canopy support structure compared to clean configuration surface pressure measurements for Mic 8. Wall jet edge velocities shown are a) 6.3 m/s and b) 20.4 m/s

Results for Canopy Configuration 1 (rod diameter 1mm, 66% open area ratio)

This canopy configuration, when placed 4 mm from the wall, most closely resembles the unidirectional canopy 3 tested by Clark *et al* (2016), but without the leading edge structure he used. Figure 11 compares wall pressure spectra measured under this canopy (at $h = 4$ mm), with the clean-wall spectra, for boundary layer edge velocities U_m of 6.3 to 24 m/s. The measurements, made at Δx=95.3 mm ($\Delta x/h$ =21.9), highlight some important effects of the canopy. Firstly, there is broadband reduction in the pressure fluctuation levels compared to the clean wall at all the speeds tested. Secondly, the attenuation curve has two parts. At low frequencies (< 200 Hz at U_m =6.3m/s, < 1kHz at U_m = 24 m/s) attenuation levels increase with frequency, reaching an inflection or maximum of 3 to 4 dB. Attenuation then holds steady (at low speed) or drops by up to 2 dB (at 24 m/s) to reach a minimum that occurs around 4 kHz at 24 m/s. The attenuation then rapidly increases with frequency reaching a maximum measured value of about 8dB at 6.3 m/s. This rapid increase occurs in the region of the pressure spectrum where it is rolling off due to dissipation effects. Figure 11b shows not only that the attenuation curves shift to higher frequency with increase in flow speed, the also show that this rightward shift is more rapid in the high-frequency region than it is in the low frequency region. This implies that the two regions have different frequency scaling, and thus presumably different physical mechanisms.

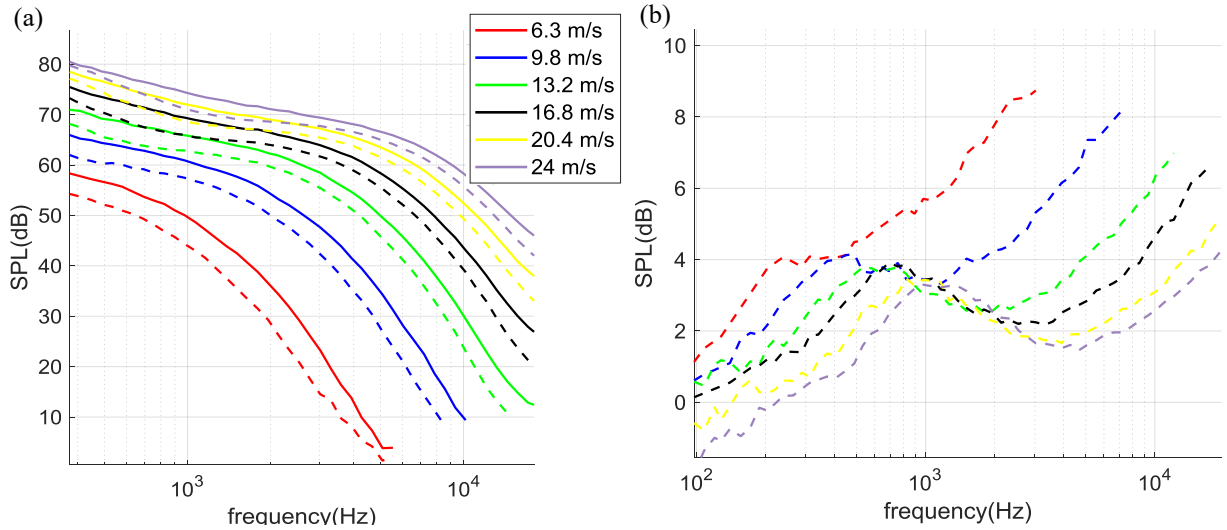

Figure 11 (a) SPL and (b) attenuation (ΔSPL) spectra vs frequency (Hz) showing comparison of surface spectra for clean wall (solid lines) and canopy configuration 1 (dashed lines) at h=4mm height, measured at Δx=95.3 mm ($\Delta x/h$ =21.9) for six different flow speeds.

Figure 12 shows spectra at the same streamwise location (Δx=95.3 mm) as the canopy height is varied with U_m = 16.8 m/s. Similar results and trends are seen at all other speeds. We see that for the same absolute streamwise distance from the canopy leading edge, the canopy effectiveness appears in general to reduce with increasing canopy height, h. For all canopy heights h, except 2mm, the attenuation spectra have the same broadband form as that seen in Figure 11b with distinct low and high frequency regions. The low frequency attenuation peak shifts downward in level and leftward to lower-frequencies as the canopy height is increased. At high frequencies, the attenuation levels are seen to drop with canopy height but there is no clear frequency shift. The exceptional case in Figure 12 is the canopy at h =2mm which shows a different attenuation pattern with changing frequencies compared to canopies at other heights. For this case, there is a small increase in surface pressure fluctuations (i.e. a negative attenuation) at lower frequencies up to 800 Hz. Above this frequency however the canopy becomes quite effective in suppressing surface pressure fluctuations, the attenuation rising sharply at higher frequencies to a maximum measured value of 9 dB at 15 kHz.

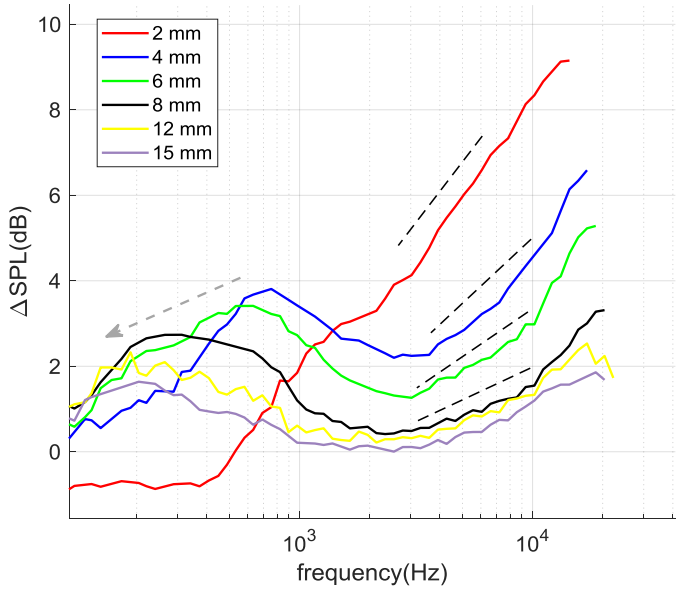

Figure 12. Attenuation (ΔSPL) vs frequency (Hz) for canopy configuration 1 at an edge velocity of 16.8 m/s at canopy heights of 2, 4, 6, 8, 12 and 15mm. The measurements shown at taken at Δx=95.3mm.

Another important aspect is the development of attenuation with streamwise distance. As an example, Figure 13 shows a series of attenuation spectra measured from the canopy leading edge ($\Delta x = 0$) to 127-mm downstream ($\Delta x/h$=31.8) for canopy height h of 4mm and U_m = 16.8 m/s. At the canopy leading edge, there is no significant attenuation of the wall pressure indicating there is no significant canopy influence on the incoming flow. With distance downstream, we see the two distinct regions of attenuation developing. In the region of the low frequency maximum, up to about 2 kHz, the attenuation rises with downstream distance, reaching a steady state by Δx=71.4 mm, $\Delta x/h$=17.9. Once this saturation value is reached, there is no further effect of streamwise position. At high frequencies beyond 2 kHz, the attenuation level increases continually with streamwise distance and there is no saturation observed. Qualitatively similar variations are seen for other canopy heights and flow speeds.

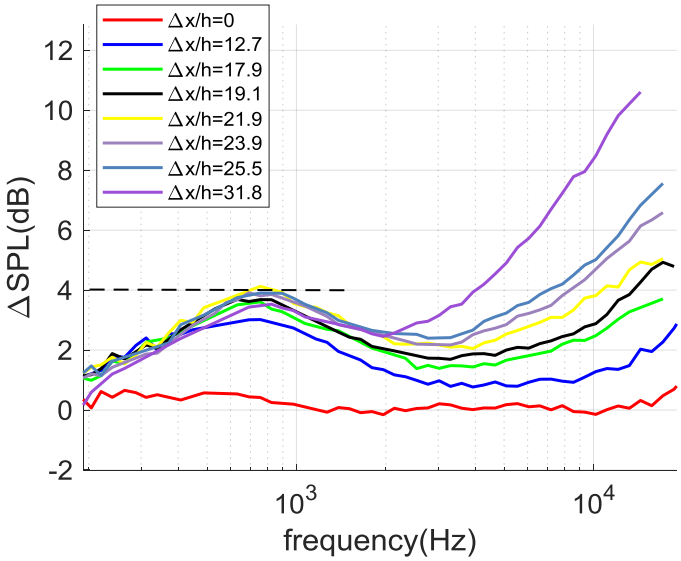

Figure 13 Attenuation (ΔSPL) vs frequency (Hz) for canopy configuration 1 for increasing streamwise distances from canopy leading edge, at U_m= 16.8 m/s and h=4mm

Attenuation Scaling for Canopy 1

Low frequency region

At lower frequencies we find that, once saturated downstream of the leading-edge region, the pressure attenuation for a substantial range of canopy heights and for all flow velocities is invariant when plotted against frequency

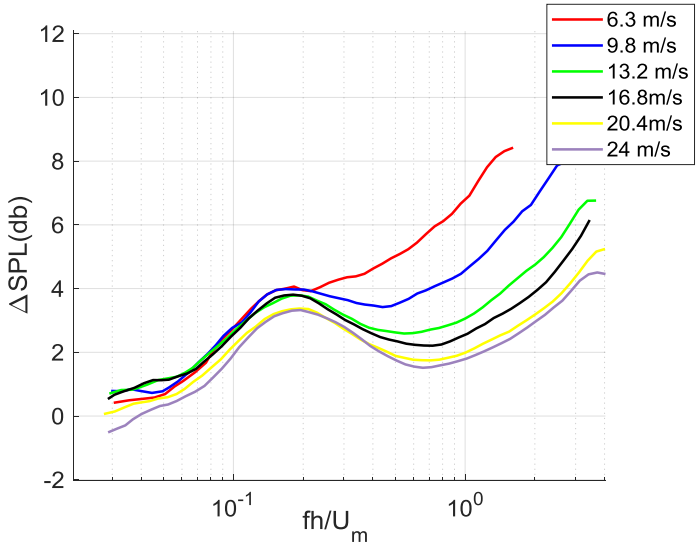

Figure 14. Attenuation plotted against frequency normalized on canopy height and boundary layer edge velocity at leading edge for canopy configuration 1 with h=4mm and Δx=95.3mm ($\Delta x/h$=21.9), for different flow velocities.

normalized on canopy height and edge velocity (fh/U_m). Furthermore, we find that in the leading-edge region the low-frequency attenuation spectrum is only a function of $\Delta x/h$ when plotted against fh/U_m. As an example of this frequency scaling, Figure 14 shows the attenuation spectra of Figure 11 (h = 4 mm, $\Delta x/h$ =21.9) vs fh/U_m. The low-frequency portions of the spectra collapse well at least up to the maximum in the low-frequency attenuation, of 3 to 4dB, that occurs near $fh/U_m = 0.18$. No significant attenuation is observed below fh/U_m of ~0.04. Attenuation spectra in the high frequency region clearly do not scale in this way. This Strouhal number scaling is potentially

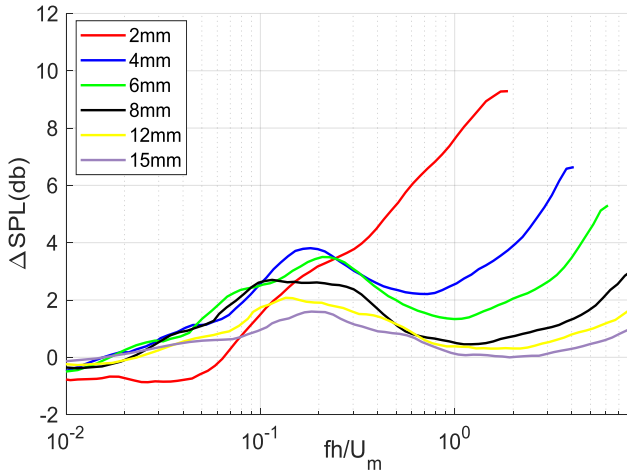

Figure 15. Comparison of attenuation scaled with non-dimensional frequency, fh/U_m for canopy configuration 1 at different heights h, measured at Δx=95.3mm U_m= 16.8 m/s.

consistent with shear sheltering mechanism, and the displacement of turbulence away from the wall. It occurs at frequencies that imply convective scales much greater than the canopy height.

Figure 15 shows the attenuation spectra of Figure 12 measured at Δx=95.3mm for different canopy heights vs fh/U_m. The low frequency portions of the attenuation spectra for canopies of all heights other than 2mm appear aligned in frequency, but not level, when scaled in this way. Instead, the level of the low frequency maximum appears to reduce with increase in canopy height starting about h = 8 mm. However, this occurs because the length of the leading-edge region scales on h, and for these larger heights the location of these measurements Δx=95.3mm is within that region. This is illustrated in Figure 16 which shows the maximum attenuation of the low frequency peak plotted against $\Delta x/h$ for all the canopy heights above 2mm. Results are shown for U_m = 16.8 m/s, but are consistent at other speeds. We see that the peak attenuation levels fall on a single curve when normalized in this way, with the attenuation

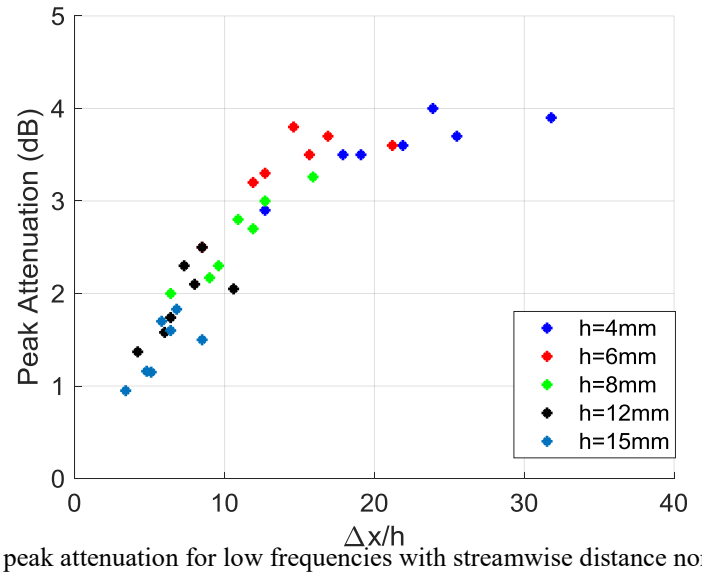

Figure 16 Variation of peak attenuation for low frequencies with streamwise distance normalized on canopy height for canopy configuration 1

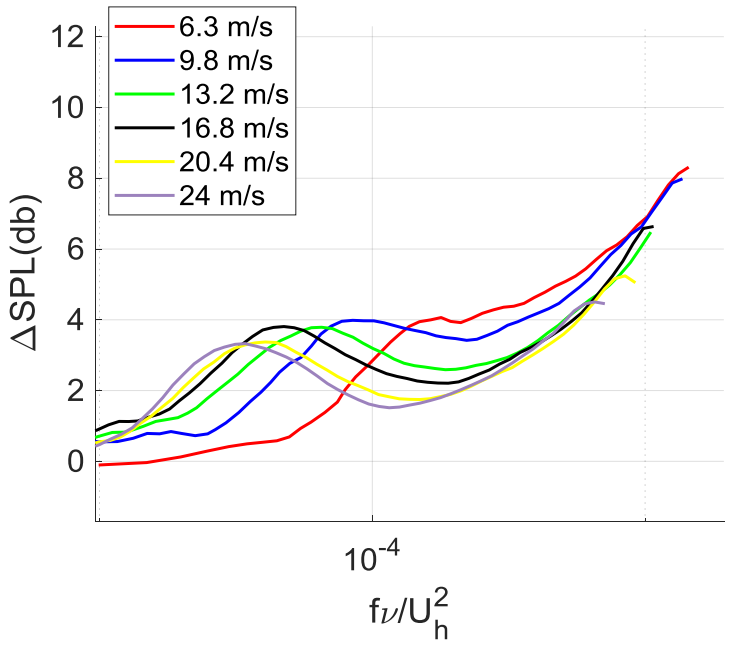

Figure 17: Scaled attenuation plotted against frequency normalized on canopy height and boundary layer edge velocity at leading edge for canopy configuration 1 showing in Figure 14, at h=4mm and Δx=95.3mm ($\Delta x/h = 21.9$), for U_m of $6.3 - 24$ m/s

rising with distance downstream, reaching a steady saturated state beyond about $\Delta x/h \approx 15$, where the peak attenuation reaches 3.5 to 4dB. Figure 16 also shows that for canopy heights 8mm and higher, Δx=95.3mm (and indeed all the streamwise measurement locations) are within the leading-edge region. This clearly indicates that the transition period scales with ratio of streamwise distance from leading edge to canopy height.

High frequency scaling

Some collapse of attenuation spectra measured at different flow speeds, in the high frequency region above 2 to 5 kHz, is obtained when plotted with frequency normalized on kinematic viscosity ν and local velocity at canopy height U_h. Figure 17 shows attenuation spectra measured at Δx=95.3mm ($\Delta x/h = 21.9$) plotted vs $f\nu/U_h^2$ for U_m ranging from 6.3 to 24 m/s. With this scaling, the rapid increase in attenuation occurs at about the same frequency

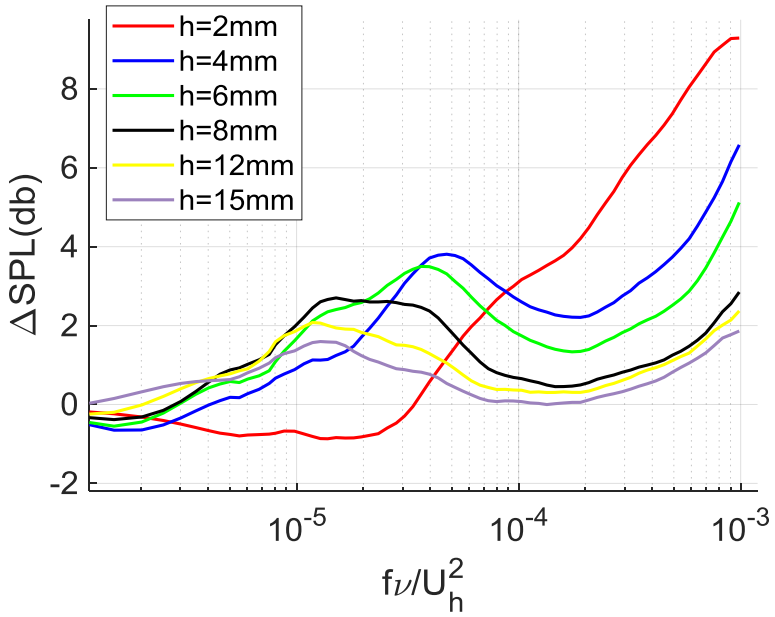

Figure 18: Scaled attenuation plotted against frequency normalized on canopy height and boundary layer edge velocity at leading edge for canopy configuration 1 shown in Figure 14, at x=95.3mm and U_m of 16.8 m/s

($fv/U_h^2 \approx 10^{-3}$) for all flow speeds. The spectra appear to be converging in this region, though it is not clear if this collapse would continue at higher frequencies. Scaling frequency on frictional velocity, u^* instead of U_h showed similar collapse of attenuation spectra for velocities higher than 13.2 m/s but did not work as well for lower velocities. These viscous scalings, which apply to a frequency range implying convective scales that are small compared to the canopy height, suggest that a dissipation mechanism is behind the high frequency attenuation, perhaps as proposed by Lilley (1998).

Figure 18 shows attenuation spectra measured at this same location and velocity, as a function of canopy height, vs. frequency normalized as fv/U_h^2. No collapse of the spectra is seen at high frequencies in this case. Instead there is a monotonic reduction in attenuation with increase in canopy height. We observe approximately the same slope for attenuation for all heights which indicates there may exist a suitable magnitude scaling for attenuation level based on canopy height.

Analysis of scaling effects in the high frequency region remains very much underway. Current work shows that, normalized as fv/U_h^2, for increasing downstream distance measured at the same canopy height, there an increase in attenuation observed. There seems to be dominant effect of streamwise distance normalized on canopy height on the attenuation levels.

Effects of Open Area Ratio and Canopy Scale

Another factor that appears to be important is the open-area ratio, $(1 - d/s)$. Figure 19 compares attenuation spectra with scaled frequency, fh/U_m for canopy configurations 1 (solid lines) and 3(dashed lines). These canopies are identical except for the difference in rod spacing s and thus open area ratio, which is 0.66 and 0.75 respectively. Spectra are shown for canopy heights h of 4mm and $U_m = 16.8\ m/s$, for varying streamwise distance normalized on canopy height, $\Delta x/h$. For the higher open area ratio at the same $\Delta x/h$, we observe a broadband reduction in attenuation. With an increased open area, the flow passes through the canopy with less resistance thereby reducing the effectiveness of canopy. At a macro scale, the canopy appears to have a homogenized effect defined by its open-area ratio thus altering the pressure difference and the strength of shear layer formation. At $fh/U_m > 1$, the attenuation slope for configuration 1 is relatively steeper with a difference of 0.8 dB fh/U_m=1 and 2.2 dB at fh/U_m=3 for $\Delta x/h =$ 25.5.

Figure 19 compares similar results for canopy configurations 1 and 2. These have the same 0.66 open area ratio but both the rod size and spacing for canopy 2 are is scaled up by 1.58 compared to canopy 1. At lower normalized frequencies up to fh/U_m=0.5, the attenuations for both configurations are effectively identical, to within 0.5dB. For fh/U_m>0.5, attenuation slope of configuration 1 is relatively steeper resulting in the difference in attenuation to increase with frequency. This indicates that additional to the open-area ratio, there is an effect of physical scale in the

effectiveness of the canopy particularly at higher frequencies. Lower diameters and spacing for the same open area ratio seem to be more effective possibly because they are more effective in promoting dissipation.

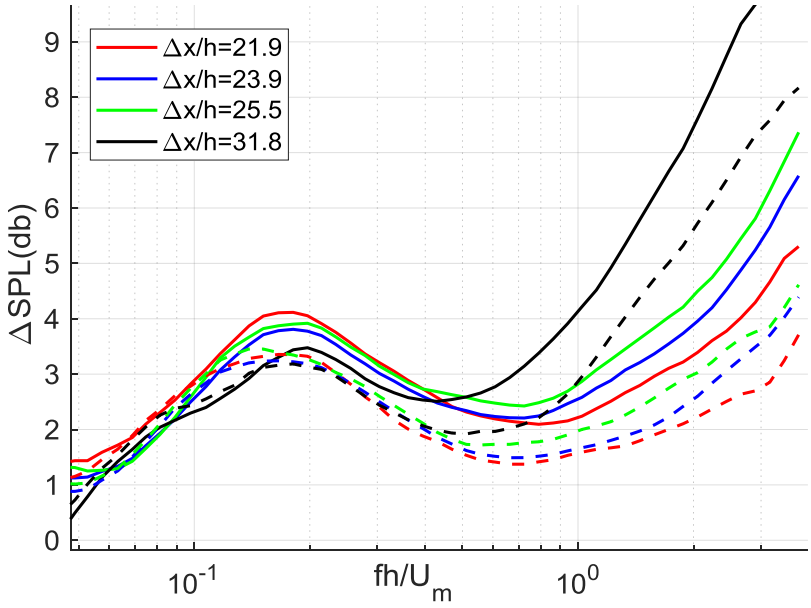

Figure 18: Comparison of attenuation vs fh/U_m at varying $\Delta x/h$ for canopy configuration 1(solid lines), and configuration 3 (dashed lines) at $h = 4mm$ $U_m = 16.8$ m/s.

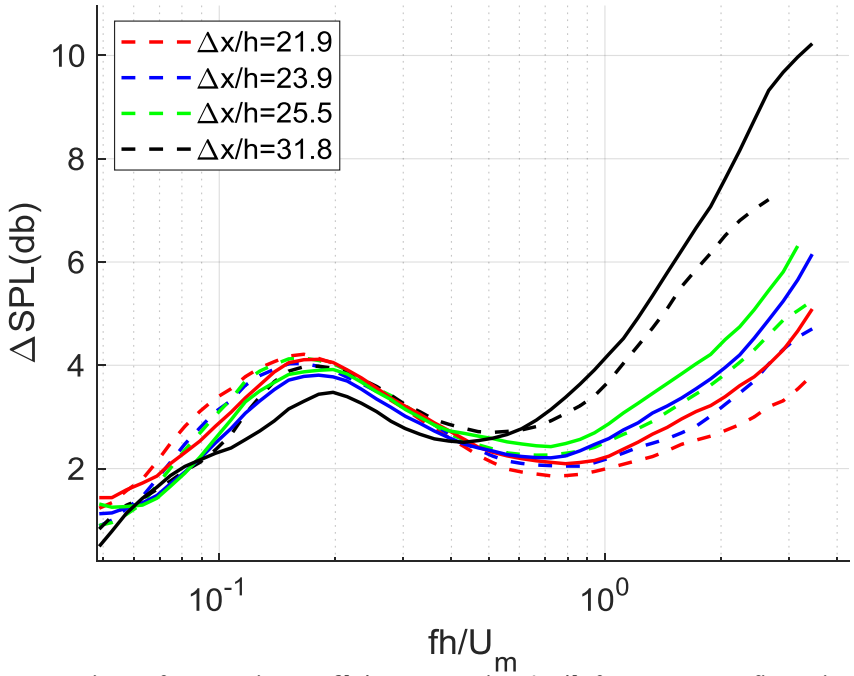

Figure 19: Comparison of attenuation vs fh/U_m at varying $\Delta x/h$ for canopy configuration 1(solid lines) and configuration 2 (dashed lines) at $h = 4mm$ $U_m = 16.8$ m/s.

V Computational Analysis

In this section we will describe a numerical/analytical model for the surface pressure spectrum attenuations that were measured in the wall jet wind tunnel. A combination of computational fluid dynamics and numerical surface pressure spectrum modeling will be used to analyze the rod canopies for their pressure attenuation performance and

effects on the flow field. We will first describe a model for the surface pressure spectrum based on the mean flow and turbulence kinetic energy (TKE) distribution in the boundary layer, and then the calculation of the mean flow field using a RANS solver will be described which gives the inputs required for the analytical model. In the following section the results will be compared to the measurements.

Surface Pressure Spectrum Numerical Model

The surface pressure spectrum can be predicted through a combination of the RANS solution data and a theoretical surface pressure model developed by Gonzalez (2019). This empirical spectrum model utilizes Blake's (1986) method of superimposing indefinitely thin harmonic waves to characterize the turbulent eddies convected across a surface in the boundary layer as the pressure source term. The pressure fluctuations on the surface can then be solved through linearized equations and a combination of the von Karman two-wavenumber velocity spectrum. Tuning of the model is required for the unknown turbulence length scales associated with the empirical velocity spectrum. In a wall jet boundary layer, Gonzalez (2019) found that two length scales were needed to capture the full spectrum which associated with the mixing and inner layers of the jet flow. The magnitude of the surface pressure fluctuations was also found to be heavily dependent upon the mean velocity gradient and turbulent vertical velocity fluctuations, especially near the wall.

The following equations summarize the surface pressure spectrum model; however, this is by no means an exhaustive review of the model. We can begin by assigning the frequency and wavenumber parameters,

$$\theta = \frac{\omega L}{U_c} \qquad \mu = k_3 L \qquad \beta = \sqrt{\mu^2 + \theta^2}$$

where U_c is the convection velocity, and L is the turbulence scale evaluated as,

$$L = \frac{1}{k_e} = \frac{L_f}{\sqrt{\pi}} \frac{\Gamma(5/6)}{\Gamma(1/3)} \tag{9}$$

where L_f is the longitudinal integral scale, Γ is a gamma function, and k_e is the wavenumber scale of the largest eddy. The length scale, L_f, is a key term in the evaluation of the surface pressure fluctuations and was found to scale on certain boundary layer length scales associated with two regions in the wall jet boundary layer. The total magnitude of the harmonic waves is a function of the gradient of streamwise velocity, the vertical fluctuating velocity, and an exponential decay term dependent upon frequency and distance from the wall. The total source of these indefinitely thin waves is integrated over the domain, and given by:

$$\mathrm{I}(\beta) = \int_0^\infty \frac{\partial U_1}{\partial y_o} \overline{v'} e^{-\frac{\beta y_o}{L}} dy_o \tag{10}$$

where U_1 is the streamwise velocity, $\overline{v'}$ is the r.m.s. of the vertical fluctuating velocity, and y_o is the distance of the harmonic layer normal to the wall. The exponential term in this equation provides a key insight into how higher frequency surface pressure fluctuations can be attenuated by either decreasing the turbulent vertical velocity fluctuations, reducing the velocity shear near the wall, or by a combination of both. These mechanisms for attenuation were hypothesized by Clark *et al.* (2016, 2017) and proven to be a key mechanism by Gonzalez (2019) and Bodling *et al.* (2018). A von Karman spectrum is used to model the energy spectrum function of the homogeneous turbulence in the boundary layer. After incorporating this into the surface pressure spectrum model, it can be simplified as a function which must integrated over all μ values in the harmonic layer.

$$F(\theta) = 2 \int_0^\infty \frac{\mathrm{I}^2(\beta)}{(1+\beta^2)^\alpha} \cdot f_L(\beta) \cdot f_\eta(\beta) d\mu \tag{11}$$

Where α is a von Karman spectrum constant equal to $7/3$. The two shape functions, f_L and f_η were proposed by Pope (2000) and used to capture the energy containing and viscous dissipation ranges, respectively, of the spectra.

$$f_L(\beta) = \left(\frac{\beta}{[(\beta)^2 + c_L]^{1/2}} \right)^{\frac{5}{3} + p_o} \tag{12}$$

$$f_\eta(\beta) = \exp\left(-\beta_\eta \left[\left(\frac{\beta\eta}{L} \right)^4 + {c_\eta}^4 \right]^{1/4} - \beta_\eta c_\eta \right) \tag{13}$$

$$\eta = \left(\frac{\nu^3}{\varepsilon} \right)^{1/4} \tag{14}$$

where η is given by the Kolmogorov length scale. Gonzalez (2019) found that shape function model constants take the values of $c_L = 3$, $p_o = 2$, $c_\eta = 0.2$, and $\beta_\eta = 10$, for a wall jet boundary layer. The one-sided surface pressure spectrum can be given as:

$$G_{pp}(\theta) = \frac{8CL{\rho_o}^2}{U_c} \theta^2 \cdot F(\theta) \tag{15}$$

Where C is a von Karman spectrum constant equal to $4\pi/9$ and ρ_o is the density of the fluid. It was found that a wall jet boundary layer must be described by two scaling regions. An outer region which dominated lower frequencies surface pressure fluctuations, and an inner scaling region which contains a high energy region dominated by large frequencies. Therefore, the total surface pressure spectrum takes the form,

$$G_{pp,t}(\theta) = G_{pp,o}(\theta) + G_{pp,i}(\theta) \tag{16}$$

The inner and outer regions scale with the following values in a turbulent wall jet:

$$L_{f,o} = y_{1/2} \qquad L_{f,i} = \theta \qquad U_{c,o} = 0.6U_m \qquad U_{c,i} = 10u_t$$

Where U_m is the maximum velocity in the boundary layer and u_τ is the friction velocity. The total surface sound pressure level then becomes:

$$SPL(\theta) = 10 \cdot \log_{10}\left(\frac{G_{pp,t}(\theta)}{(20\times10^{-6})^2}\right) \tag{17}$$

The evaluation of the surface pressure spectrum model provides understanding of the fundamental mechanisms behind the production of surface pressure fluctuations. With the knowledge that the magnitude of the pressure fluctuations on the wall are a directly function of the velocity shear, vertical fluctuating velocity, the length scales of the turbulent eddies and the velocities at which they are convected, allows for these canopy structures to be optimized for surface pressure attenuation.

Computational Model

A computational model of the rod canopy under investigation was developed and shown in Figure 20. The rod canopy can be modeled using a single rod with periodic boundary conditions placed at the centerlines between the rods ($z = 0$ & $z = s$). This reduces the computational expense of the analysis, while still representing the spanwise behavior of the rod canopy. The model is analyzed through RANS calculations via ANSYS Fluent. A standard $k-\epsilon$ turbulence model with a standard wall treatment was used in the simulation. The inlet boundary condition ($x = 0$ & $y = 200$) was assigned as a velocity inlet with user defined velocity components, turbulent kinetic energy, and turbulent dissipation rate profiles. These profiles were found through a separate CFD analysis of the experimental wall jet wind tunnel facility performed by Gonzalez (2019). A pressure outlet boundary condition was places at $x = 552\ mm$. A wall condition was assigned to the surface of the rod and at $y = 0$. The total model consists of 5.9×10^6 elements.

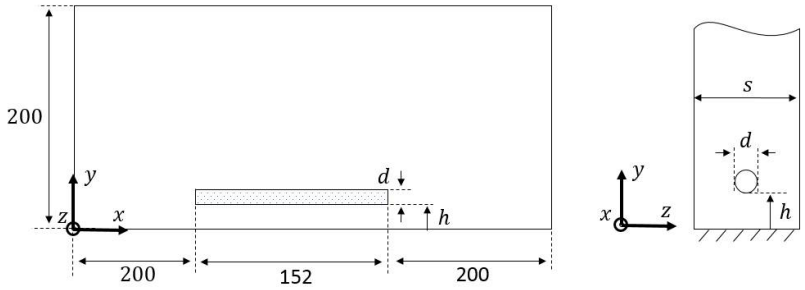

Figure 20: Computational model of rod canopy. All dimensions are in mm.

As discussed previously, the vertical fluctuating velocity component is required for the prediction of the surface pressure spectrum. Since RANS calculations only provide the averaged turbulent kinetic energy, an anisotropic correction function developed by Gonzalez (2019) was used for a wall jet boundary layer in order to estimate the vertical fluctuating velocity profiles. This correction function was tuned to match computational surface spectrum predictions to the measured results, and takes the form:

$$\left[\overline{v'^2}\right]_{TBL} = \left[a + b\left(\frac{y}{y_{1/2}} - 0.8\right)^c\right] \cdot \left[\frac{2}{3}k\right] \tag{18}$$

where $\left[\overline{v'^2}\right]_{TBL}$ is the corrected fluctuating vertical velocity, k is the turbulent kinetic energy, $y_{1/2}$ is the mixing layer height, y is the profile position normal to the wall, and *a, b,* and *c* are model constants which were found to be equal to 0.3, 0.0938, and 2, respectively.

The rod canopy can also be modeled as a homogenous layer of porous material. Computational analysis of homogenous porous canopies for acoustic pressure shielding has been previously been performed using properties equivalent to an owl's downy hairs on its wing (Gonzalez 2019). However, direct estimation of an equivalent porous canopy based on the physical rod canopy dimensions has not been performed. This allows for a simplified model of the canopy while still accounting for the density (or porosity) of the rods in the canopy layer and the viscous resistance that they exert on the flow. Simpler models of the canopies can be created and applied to various engineering applications and reduce the overall computational expense of the analysis. The computational model of the porous canopy will be of the same dimensions as shown in Figure 20, with the exception of a homogenous porous layer extending across $z = 0 \rightarrow s$, instead of the rod. The boundary conditions of the model will also remain the same as the rod canopy model. The porosity, γ, of the porous layer based on the dimensions of the rod canopies can be given as:

$$\gamma = 1 - \frac{\pi d}{4s} \tag{19}$$

The component viscous resistances, ψ_i, can be empirically estimated by the following relations (Sangani and Acrivos 1982, Drummond and Tahir 1984):

$$\frac{k_1}{a^2} = \frac{1}{4\phi}\left(-\ln\phi - 1.476 + 2\phi - \frac{\phi^2}{2} + O(\phi^4)\right) \quad (20)$$

$$\frac{k_2}{a^2} = \frac{1}{8\phi}\left(-\ln\phi - 1.490 + 2\phi - \frac{\phi^2}{2} + O(\phi^4)\right) \quad (21)$$

where $\psi_i = 1/k_i$, a is the rod radius, $\phi = 1 - \gamma$, and $\psi_3 = \psi_2$.

Table 5: Viscous properties of rod canopy configurations for an equivalent porous layer

Configuration	d (mm)	s (mm)	γ	ψ_1 (m^{-2})	ψ_2 (m^{-2})
1	1.00	3.00	0.74	1.18 (10^7)	2.47 (10^7)
2	1.58	4.76	0.74	4.70 (10^6)	9.79 (10^6)
3	1.00	4.00	0.80	5.98 (10^6)	1.23 (10^7)

Rod Canopy Flow Results

Computational analyses of the rod style canopies experimentally tested was performed. This section outlines the general flow field results of rod canopy configuration 1, which corresponds to rod canopy dimensions of $d = 1\ mm, s = 3\ mm, h = 4\ mm$ at a leading edge velocity of $U_m = 16.8\, m/s$. The streamwise velocity profile of the rod canopy can be seen in Figure 21 (Top) which are taken at the center plane between two rods ($z = 0$). The canopy begins at $\Delta x/h = 0$ and its boundaries are outlined as black dashed lines. The contour is normalized by U_m taken at $\Delta x/h = 0$. A velocity deficit region is created beneath the canopy which gradually increases in size with distance downstream. A high level of velocity deficit can also be seen at the height of the rod canopy. This can be clearly seen in Figure 22 (Left), which shows the spanwise distribution of the streamwise velocity taken at $\Delta x/h = 24$ (Mic 6). A formation of a boundary layer is present on the surface of the rods, which is to be expected. Due to each rod in the canopy creating a shear layer, the streamwise velocity will be significantly reduced at the height of the canopy, which can be seen Figure 23 of the velocity profile compared with a clean wall. Above the rod, the profile takes on a typical boundary layer profile. This region of slower velocity decreases the velocity shear near the wall which will effectively reduce the magnitude of the I function in Equation 10, therefore, attenuating the surface pressure spectrum levels.

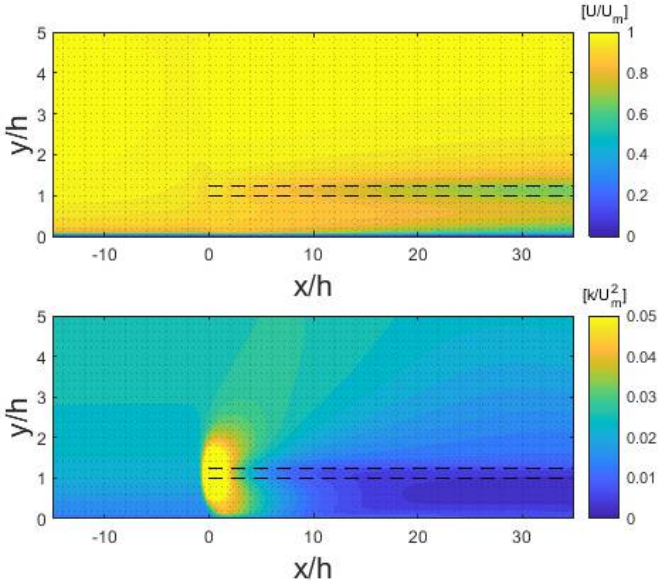

Figure 21: Streamwise velocity contour (Top) and turbulent kinetic energy (Bottom) of rod canopy

The normalized turbulent kinetic energy contours can be seen in Figure 21 (Bottom). A large production of TKE is present at the leading edge of the rod canopy, due to the physical impact of the rods on the flow. A more streamlined design would reduce this effect. With distance downstream, the initial TKE produced at the leading edge is dissipated and lower levels of turbulence are present beneath the canopy. Higher levels of TKE are present above the canopy

therefore, the rod canopies are effectively shielding the wall from the turbulence in the flow. The spanwise distribution of turbulent kinetic energy at $\Delta x/h = 24$ (Mic 6) can be seen in Figure 22 (Right). Higher levels of turbulence remain present on the rod's surface and the wall of the test plate due to the velocity shear of the boundary layers. Nevertheless, the rods clearly demonstrate a turbulence shielding effect and acoustic attenuation is expected to be present due to the reduction of turbulence near the wall. When looking at the tke profile taken at $\Delta x/h = 24$, we can see the tke is significantly reduces as compared with the clean wall case. Based on the empirical model of the surface pressure fluctuations, reduction in the fluctuating velocity near the wall will lead to attenuated surface pressure fluctuations. We can expect to observe attenuation in surface pressure fluctuations based on reduced turbulence near the wall and the presence of the velocity deficit region.

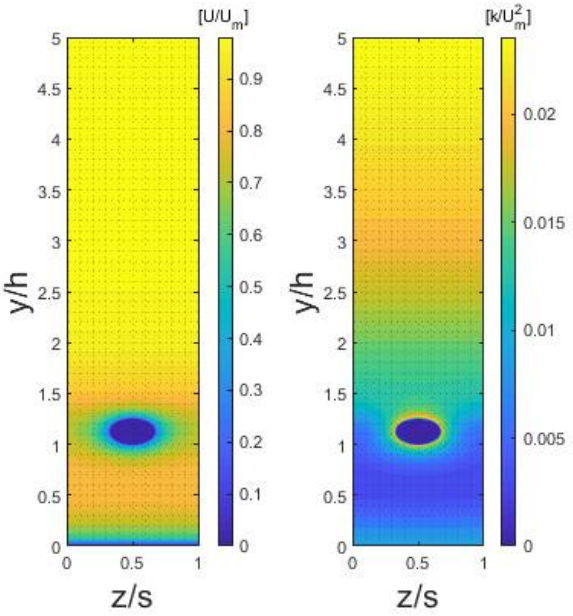

Figure 22: Spanwise view of streamwise velocity (Left) and TKE (Right) contours at $\Delta x/h = 24$

Porous Canopy Flow Results

A computational analysis was performed using an equivalent porous canopy modeled after configuration 1 of the rod canopy. The physical properties of the porous media used in this RANS calculation can be found in Table 5. Normalized streamwise velocity profiles taken at microphone 6, $\Delta x/h = 24$, can be seen in Figure 24 (Top). A velocity deficit region is created due to the influence of the porous canopy; however, it is not of the equal magnitude to the case where the physical rods are modeled. The boundary layer shear layer that was formed on the solid surface of the rods is not captured through the estimation of a porous canopy, even with equivalent viscous properties. The turbulent kinetic energy also does not resemble the same behavior as the rod case. Attenuation of the tke is only present very close to the wall. The physical structure of the rods and the formation of the shear layer on its surface plays a major role in the velocity shear and turbulent kinetic energy deficit of these canopy structures. Although the porous canopy does not show as great of an influence on the velocity shear and tke profiles, we should still expect an attenuation in surface pressure fluctuations do the dominance of these terms in the empirical surface pressure model.

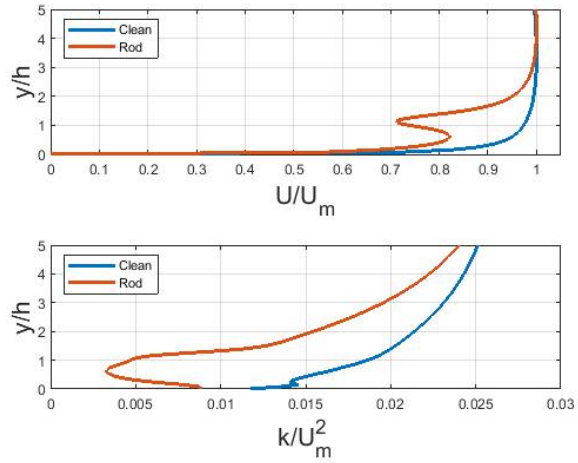

Figure 23: Normalized streamwise velocity (Top) and turbulent kinetic energy (Bottom) profiles at $\Delta x/h = 24$ for rod canopy configuration 1

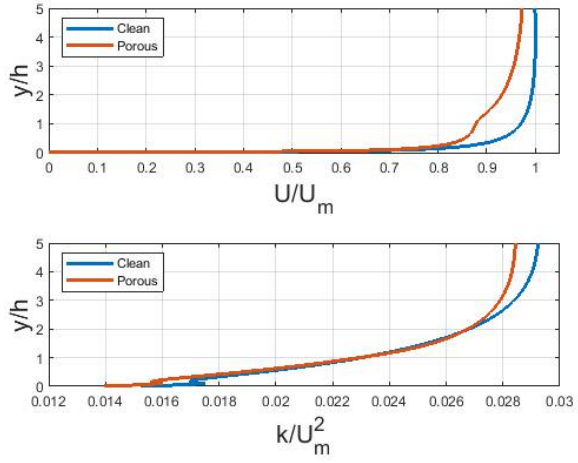

Figure 24: Normalized streamwise velocity (Top) and turbulent kinetic energy (Bottom) profiles at $\Delta x/h = 24$ for an equivalent porous canopy

Spectral Analysis: Configuration 1

An analysis of the surface pressure spectrum was performed on the RANS solutions of the clean and rod canopy models. This section outlines the numerical spectral results of canopy configuration 1, which corresponds to rod canopy dimensions of $d = 1\,mm, s = 3\,mm, h = 4\,mm,$ and $U_m = 16.8\,m/s$. Spectral analysis was performed at

the centerline between the rods at all microphone locations. The predicted surface sound pressure level spectrum and corresponding SPL attenuation levels for the clean and rod canopy for configuration 1 taken at Mic 6 ($x = 95.3\,mm$, $\Delta x/h = 24$) can be seen in Figure 25, as compared with experimentally measured results. The prediction of the surface pressure spectrum for the clean wall shows relatively good agreement with the experimentally measured results. The surface pressure prediction model captures the overall behavior of the spectra, with only slight over predictions for frequencies associated with the inner scaling region. The rod canopy demonstrates a broadband attenuation of the surface pressure spectrum. Two SPL attenuation peaks were found to be present with the rod canopies, and are properly captured by the computational analysis of the canopies. At high frequencies, a maximum attenuation of the surface SPL of about 5 dB was reached, comparing this to experimental found results of about 6.5 dB shows that the computational prediction is within a reasonable range of measured uncertainty. High SPL attenuation is observed at higher frequencies because this part of the spectrum is dominated by the inner scaling region. The velocity shear and turbulence deficit created by the rod canopy within the inner scaling region of the wall jet boundary layer gives the high frequency attenuation of surface sound pressure levels. Lower levels of attenuation are found at lower frequencies, which is to be expected since this is controlled by the outer scaling of the wall jet boundary layer and the canopy demonstrates little effect on this portion of the flow.

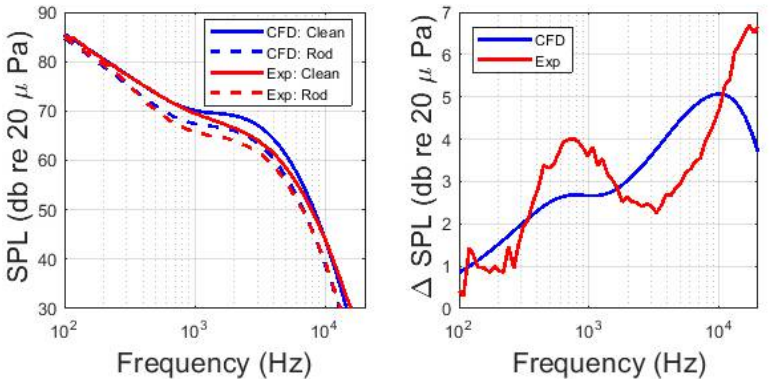

Figure 25: Numerical prediction of surface pressure spectrum for rod canopy configuration 1 at microphone 6 for a $U_m = 16.8\,m/s$

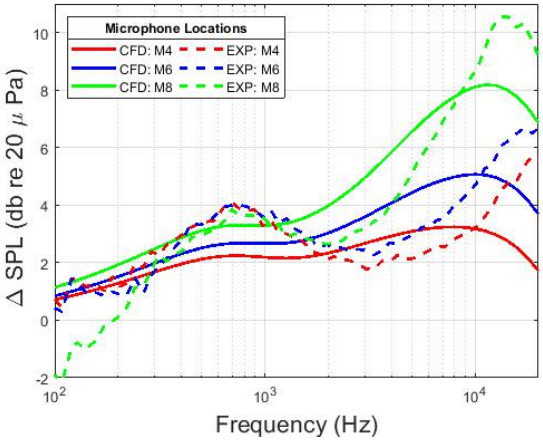

Figure 26: Surface SPL attenuation at microphone locations of computational and measured results for rod canopy configuration 1 at a $U_m = 16.8\,m/s$

We can also compare the computational results with the evolution of surface SPL attenuation with distance downstream. Figure 26 shows the computational and measured results of the surface SPL attenuation at microphones 4, 6, and 8. The SPL attenuation increases with distance downstream for both the computational and measured results in a consistent fashion. This effect was first observed experimentally by Clark (2107) and later computationally found by Gonzalez (2019). Overall the computational results capture the same behavior as the measured results, with slight discrepancies present in the peak magnitude regions of attenuation, located at 1 kHz and 10 kHz.

Further tuning of the surface pressure fluctuation model can be performed in order to adjust for discrepancy between the experimental and measured results. The current model is tuned for a clean wall jet boundary layer, which has shown to provide an accurate representation of the clean wall spectra. However, some of the model's aspects, such as the viscous dissipation shape function, anisotropic fluctuating velocity correction function, inner length turbulence length scale definition, inner scaling convection velocity were taken to be the same as the clean wall case. Although the model's current use of these parameters gives a good estimate of the surface pressure fluctuations with a canopy, there is still prospect for improvement. Experimental measurements and unsteady CFD calculations of the parameters used in the model can provide higher confidence for the use of these model features and therefore will improve the accuracy of the computational predictions of the acoustic shielding effects of the rod canopies.

Spectral Analysis: Configuration

The predicted surface SPL attenuation levels for the rod canopy configuration 3 taken at Mic 6 ($x = 95.3\,mm$, $\Delta x/h = 24$) and $U_m = 16.8\,m/s$ can be seen in Figure 26, as compared with experimentally measured results. The results are also compared with those for rod configuration 1. It can be seen that the numerically calculated acoustic performance at high frequencies for rod configuration 3 is less than that of configuration 1. This is the same trend which was observed through experimental measurements. Since the rods in configuration 3 are "less dense" than configuration 1, the canopy exerts less resistance on the flow. This was quantitatively found through estimating the

porosity and viscous resistance of the rod canopy, which can be seen in Table 5. Configuration 3 demonstrates less viscous resistance and increased porosity than the rod configuration 1. Gonzalez (2019) has previously found that these two parameters play a key role in the acoustic performance of pressure shielding canopies, and is further supported in this study. The distinction between the acoustic performance between configuration 1 and 3 increases with frequency. This is due to the fact that the higher frequency region of the surface pressure spectrum is controlled by the flow very close to the wall. With the canopies having the greatest influence near the wall, typically in the range of the canopy height, the greatest acoustic performance difference experienced at high frequencies. A maximum attenuation of the surface SPL of about 4 dB was calculated, comparing this to experimental found results of about 5 dB shows that the computational prediction is within a reasonable range of measured uncertainty. The low frequency attenuation peak is also captured within 0.5 dB of the measured results.

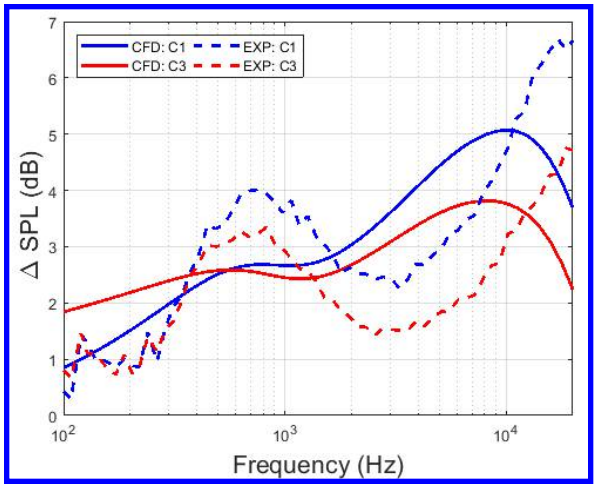

Figure 26: Comparison of surface SPL attenuation at microphone location 6 of computational and measured results for rod canopy configuration 1 and 3 for a $U_m = 16.8\,m/s$

Spectral Analysis: Equivalent Porous Canopy

An analysis of the surface pressure spectrum was performed on the RANS solutions of the clean an equivalent porous canopy model. This section outlines the numerical spectral results of a porous canopy with equivalent properties to rod canopy configuration 1, which corresponds to rod canopy dimensions of $d = 1\,mm, s = 3\,mm, h = 4\,mm,$ and $U_m = 16.8\,m/s$. The viscous resistance properties for the equivalent porous canopy used in this study can be found in Table 5. The predicted surface SPL attenuation levels for the equivalent porous canopy taken at Mic 6 ($x = 95.3\,mm$, $\Delta x/h = 24$) and $U_m = 16.8\,m/s$ can be seen in Figure 27, as compared with the computational and experimental results of rod configuration 1. Attenuation of the surface SPL is observed over the broadband for the equivalent porous canopy. The general behavior of attenuation at high frequencies is captured with use of the equivalent porous canopy. A maximum attenuation of about 5 dB is calculated for the porous canopy, which is the same range that was found with the rod canopy, both computationally and experimentally. The equivalent porous canopy does not capture the lower frequency attenuation peak as well as the physical modeled rods do. The formation of the boundary layer on the rod's surface, and the interaction these have on the overall canopy plays a key role in the modeling the attenuation at this frequency range. The viscous resistance formulation based on the geometry of the rod canopy seems to provide a good estimate of the pressure shielding performance of the canopy however, there may exist better empirical estimates which were not used in this present study. Another aspect which may be at play is the homogenization of attenuation across the spanwise direction. The surface pressure fluctuations measurements in this study were taken at the centerline between the rods. The surface SPL attenuation directly beneath the rods may be of a different magnitude and could resemble the homogenized porous canopy estimated better, however this was not investigated in this present study. Gonzalez (2019) has also shown that the same behavioral acoustic performance trends (density of canopy, attenuation with distance downstream, height of canopy) present themselves through modeling the canopy as a porous layer.

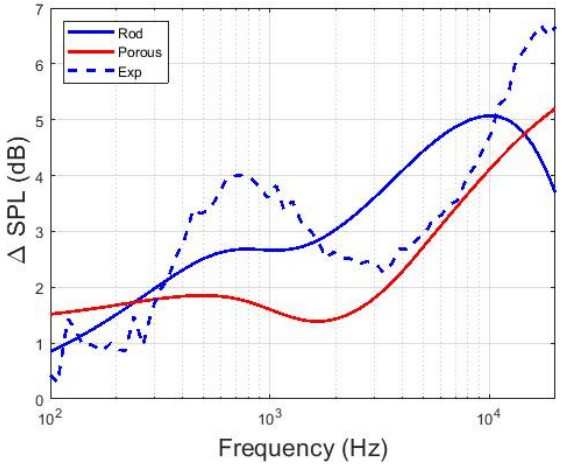

Figure 27: Surface SPL attenuation at microphone location 6 for an equivalent porous canopy compared with computational and experimental results for rod configuration 1

VI Conclusion

A combination of experimental and numerical studies was performed on elemental canopy configurations (parallel arrays of streamwise rods) that eliminate the confounding effects of a leading-edge support structure, to investigate

the fundamental mechanisms of acoustic pressure shielding. Experiments show that such a canopy produces attenuation in two distinct frequency ranges. At low frequencies below about 1 kHz, attenuation spectra scale on the canopy height Strouhal number but at high frequencies beyond 3-6 kHz, a dissipation type frequency scaling appears more appropriate. At lower frequencies, once saturated downstream of the leading edge region, the pressure attenuation for a substantial range of canopy heights and for all flow velocities is invariant when plotted against frequency normalized on canopy height and edge velocity (fh/U_m). In the leading edge region the low-frequency attenuation spectrum is only a function of $\Delta x/h$ for this scaling. This Strouhal number scaling may be consistent with shear sheltering mechanism, and the displacement of turbulence away from the wall. It occurs at frequencies that imply convective scales that are large compared to the canopy height. At higher frequencies pressure attenuation spectra are best collapsed when frequency is normalized on the kinematic viscosity and the undisturbed mean velocity at the canopy height ($f\nu/U_h^2$). This viscous scaling, which applies to a frequency range implying convective scales that are small compared to the canopy height, suggest that enhanced dissipation is a key element of the attenuation. In both frequency ranges pressure attenuation reduces with increasing open area ratio. Changing the diameter and spacing of the canopy rods, but not the area ratio, has no effect on low frequency attenuation, implying the canopy effects are homogenized here. At high frequency, however, larger rods and spacing reduce the pressure attenuation slightly, consistent with a dissipation mechanism here.

RANS calculations are performed simulating the canopy geometry directly and as an equivalent porous layer. Pressure fluctuation spectra predicted from the RANS results by separately accounting for inner and outer layer contributions are able to accurately recreate the wall pressure spectra both with and without the canopy and thus the major features of the attenuation spectra. These show the vertical fluctuating velocities and velocity shear near the wall play a dependence in the magnitude of high frequency surface pressure fluctuations. A velocity shear was created around the rod through the non-slip mechanism present on the surface of the rods. A velocity deficit region was also present beneath the canopy. Although higher turbulence production was present at the leading edge of the rod canopy, this was quickly dissipated and lower levels of turbulence were present beneath the rod canopy. The rods were effectively shielding the wall from the turbulence contained in the flow. With a decrease in the velocity shear and turbulence near the wall, attenuation in the surface pressure fluctuations should be expected due these terms dominance in the empirical formulation of the surface pressure function. Numerical spectral analysis did in fact show attenuation of surface SPL levels over the broadband for the rod configurations tested. Numerically calculated acoustic attenuation of the rod canopies were found to be within a reasonable range as compared with experimentally measured results. Identical trends with respect to distance downstream and rod spacing were found through computational analysis as was found with measured results. Modeling the rod canopies as an equivalent homogenous porous layer provides a good means of estimating the acoustic attenuation performance of the rod canopies at high frequencies.

Acknowledgments

The authors would like to thank the National Science Foundation, in particular Dr. Ron Joslin, for their support of this research under grant CBET-1802915. The assistance of and insightful discussions with Nathan Alexander, Russell Repasky, Stefan Leitica and Lorna Ayton are gratefully acknowledged.

References

Afshari, A., Azarpeyvand, M., Dehghan, A. A. and Szoke, M. (2016). Trailing Edge Noise Reduction Using Novel Surface Treatments. 22nd AIAA/CEAS Aeroacoustics Conference. Lyon, France.

Afshari, A., Azarpeyvand, M., Dehghan, A. A. and Szoke, M. (2017). Effects of Streamwise Surface Treatments on Trailing Edge Noise Reduction. AIAA Aviation 17. Denver, CO.

Belcher, S. E., Harman, I. N. and Finnigan, J. J. (2012). "The Wind in the Willows: Flows in Forest Canopies in Complex Terrain." Annual Review of Fluid Mechanics **44**(1): 479-504.

Belcher, S. E., Jerram, N. and Hunt, J. C. R. (2003). "Adjustment of a turbulent boundary layer to a canopy of roughness elements." Journal of Fluid Mechanics **488**: 369-398.

Blake, W. (1986). Mechanics of Flow Induced Sound and Vibration. Orlando, FL, Academic Press.

Bodling, A., Agrawal, B. R., Sharma, A., Clark, I., Alexander, W. N. and Devenport, W. J. (2017). Numerical Investigation of Bio-Inspired Blade Designs at High Reynolds Numbers for Ultra-Quiet Aircraft and Wind Turbines. AIAA Aviation 17. Denver, CO.

Bodling, A., Agrawal, B. R., Sharma, A., Clark, I., Alexander, W. N. and Devenport, W. J. (2017). Numerical Investigations of Bio-Inspired Blade Designs to Reduce Broadband Noise in Aircraft Engines and Wind Turbines. 55th AIAA Aerospace Sciences Meeting. Grapevine, TX.

Bodling, A. and Sharma, A. (2018). "Numerical investigation of low-noise airfoils inspired by the down coat of owls." Bioinspir Biomim **14**(1): 016013.

Bradshaw, P. and Gee, M. T. (1962). Turbulent Wall Jets with and without an External Stream, Aeronautical Research Council.

Clark, I., Baker, D., Alexander, W. N., Devenport, W. J., Glegg, S. A., Jaworski, J. and Peake, N. (2016). Experimental and Theoretical Analysis of Bio-Inspired Trailing Edge Noise Control Devices. 22nd AIAA/CEAS Aeroacoustics Conference. Lyon, France.

Clark, I. A., Alexander, W. N., Devenport, W., Glegg, S., Jaworski, J. W., Daly, C. and Peake, N. (2017). "Bioinspired Trailing-Edge Noise Control." AIAA Journal **55**(3): 740-754.

Clark, I. A., Daly, C. A., Devenport, W., Alexander, W. N., Peake, N., Jaworski, J. W. and Glegg, S. (2016). "Bio-inspired canopies for the reduction of roughness noise." Journal of Sound and Vibration **385**: 33-54.

Devenport, W. J., Grissom, D. L., Nathan Alexander, W., Smith, B. S. and Glegg, S. A. L. (2011). "Measurements of roughness noise." Journal of Sound and Vibration **330**(17): 4250-4273.

Drummond, J. E. and Tahir, M. I. (1984). "Laminar viscous flow through regular arrays of parallel solid cylinders." International Journal of Multiphase Flow **10**(5): 515-540.

Finnigan, J. (2000). "Turbulence in Plant Canopies." Annu. Rev. Fluid Mech. **32**: 519-571.

Gonzalez, A. (2019). A Computational Analysis of Bio-Inspired Modified Boundary Layers for Acoustic Pressure Shielding in A Turbulent Wall Jet. MS, Florida Atlantic University.

Hunt, J. C. R. and Durbin, P. A. (1999). "Perturbed vortical layers and shear sheltering." Fluid Dynamics Research **24**: 375-404.

Jacobs, R. G. and Durbin, P. A. (1998). "Shear sheltering and the continuous spectrum of the Orr–Sommerfeld equation." Physics of Fluids **10**(8): 2006-2011.

Kleinfelter, A., Repasky, R., Hari, N., Leitica, S., Vishwanathan, V., Organski, L., Schwaner, J., Alexander, N. and Devenport, W. J. (2019). Development and Calibration of a new Anechoic Wall Jet Wind Tunnel. AIAA Science and Technology Forum and Exposition 2019. San Diego, CA.

Kwak, R., Pham, V. S. and Han, J. (2017). "Sheltering the perturbed vortical layer of electroconvection under shear flow." Journal of Fluid Mechanics **813**: 799-823.

Lilley, G. (1998). "A study of the silent flight of the owl."

Millican, A. J. (2017). Bio-Inspired Trailing Edge Noise Control: Acoustic and Flow Measurements. MS MS, Virginia Tech.

Millican, A. J., Clark, I., Devenport, W. J. and Alexander, W. N. (2017). Owl-Inspired Trailing Edge Noise Treatments: Acoustic and Flow Measurements. 55th AIAA Aerospace Sciences Meeting. Grapevine TX.

Pope, S. B. (2000). Turbulent Flows, Cambridge University Press.

Prabha, T. V., Leclerc, M. Y., Karipot, A., Hollinger, D. Y. and Mursch-Radlgruber, E. (2007). "Influence of Nocturnal Low-level Jets on Eddy-covariance Fluxes over a Tall Forest Canopy." Boundary-Layer Meteorology **126**(2): 219-236.

Raupach, M. R., Finnigan, J. J. and Brunet, Y. (1996). "Coherent eddies and turbulence in vegetation canopies: the mixing-layer analogy." Bound. Layer Meterol. **78**(3-4): 351-382.

Sangani, A. S. and Acrivos, A. (1982). "Slow flow past periodic arrays of cylinders with application to heat transfer." International Journal of Multiphase Flow **8**(3): 193-206.

Smith, B. S. (2008). Wall jet boundary layer flows over smooth and rough surfaces. PhD, Virginia Polytechnic Institute and State University.

Wygnanski, I. J., Katz, Y. and Horev, E. (1992). "On the applicability of various scaling laws to the turbulent wall jet." Journal of Fluid Mechanics **234**: 669-690.